

High-resolution spectroscopic analysis of four unevolved barium stars*

M. P. RORIZ ¹, N. HOLANDA ¹, L. V. DA CONCEIÇÃO ², S. JUNQUEIRA,¹ N. A. DRAKE ^{1,3}, A. SONALLY,¹ AND C. B. PEREIRA¹

¹*Observatório Nacional/MCTI, Rua General José Cristino, 77, 20921-400, Rio de Janeiro, Brazil*

²*Department of Physics and Astronomy, University of Manitoba, Winnipeg, MB, R3T 2N2, Canada*

³*Laboratory of Observational Astrophysics, Saint Petersburg State University, Universitetski pr. 28, 198504, Saint Petersburg, Russia*

(Received xxxx; Revised yyyy; Accepted zzzz)

Submitted to AJ

ABSTRACT

A classical Local Thermodynamic Equilibrium analysis, based on high-resolution spectroscopic data, is performed for a sample of three potential barium dwarf candidates and one star already recognized as such. We derived their atmospheric parameters, estimated their masses and luminosities, and determined chemical abundances for a set of 21 elements, including CNO. Some elemental abundances are derived for the first time in HD 15096, HD 37792, and HD 141804. The program stars are dwarfs/subgiants with metallicities typical of disc stars, exhibiting moderate carbon enhancements, with [C/Fe] ratios ranging from +0.29 to +0.66 dex, and high levels of *slow* neutron-capture (*s*-process) elements, with [s/Fe] \gtrsim +1.0 dex. As spectroscopic binaries, their peculiarities are attributable to mass transfer events. The observed neutron-capture patterns were individually compared with two sets of *s*-process nucleosynthesis models (Monash and FRUITY), yielding dilution factors and masses estimates for the former polluting Asymptotic Giant Branch stars. Low-mass ($\lesssim 3.0 M_{\odot}$) models successfully reproduce the observations. In addition, we estimated mean neutron exposures of the order of 0.6 – 0.7 mb⁻¹ for the *s*-processed material observed in their envelopes. Applying an empirical initial-final mass relation, we constraint in $\sim 0.7 M_{\odot}$ the mass of their dim white-dwarf companions. Moreover, our kinematic study revealed that the program stars are members of the thin disk, with probabilities greater than 70%. Hence, we identified HD 15096 and HD 37792 as new barium dwarfs and confirmed that HD 141804 is a barium dwarf. Thus, the number of barium dwarfs identified in the literature from high-resolution spectroscopy increases to 71 objects.

Keywords: stars: fundamental parameters — stars: atmospheres — stars: abundances — stars: chemically peculiar — stars: individuals (HD 15096, HD 37792, HD 141804, HD 207585) — techniques: spectroscopy

1. INTRODUCTION

Barium (Ba) stars (Bidelman & Keenan 1951) and their Population II analogues, CH stars (Keenan 1942), were initially recognized as red giants enriched in car-

bon and elements synthesized mostly through the *slow* neutron-capture mechanism (*s*-process; Burbidge et al. 1957; Käppeler et al. 2011; Lugaro et al. 2023). However, the *s*-process nucleosynthesis is expected to take place in the interiors of Thermally-Pulsing Asymptotic Giant Branch (TP-AGB) stars (Gallino et al. 1998; Busso et al. 1999; Straniero et al. 2006; Karakas & Lattanzio 2014). Consequently, as first ascent giants, Ba and CH stars are not able to produce *in loco* and self-enriched their envelopes with the *s*-processed material. Until the discovery of their binary nature (McClure et al. 1980; McClure

Corresponding author: M. P. Roriz
michelle@on.br

* HD 15096, HD 37792, and HD 141804 were observed under the program ID 097.A-9024(A). HD 207585 was observed under the agreement between Observatório Nacional (Brazil) and European Southern Observatory (ESO).

1984; McClure & Woodsworth 1990), such peculiarities posed a challenge to the early stellar evolution models.

Belonging to binary systems, the chemical anomalies observed in Ba and related stars are attributed to mass exchange effects. In the framework of post-mass-transfer interacting binaries, the primary TP-AGB star loses mass and pollutes the atmosphere of its less evolved companion. As the secondary star evolves, it becomes a *s*-rich giant, observed as a Ba/CH star, depending on the metallicity, while the former TP-AGB ends as a dim White Dwarf (WD). Over the years, detailed chemical abundance analyses have confirmed the *s*-rich nature of the Ba stars (Allen & Barbuy 2006a; Pereira et al. 2011; de Castro et al. 2016; Karinkuzhi et al. 2018b; Shejeelammal et al. 2020; Roriz et al. 2021a,b) and CH stars (Goswami et al. 2006; Karinkuzhi & Goswami 2014, 2015; Goswami et al. 2016; Purandardas et al. 2019). Moreover, their binary nature is widely supported by data acquired from extensive programs of radial velocity monitoring (Jorissen et al. 1998, 2019). As post-mass-transfer binaries, Ba/CH stars provide valuable observational constraints to *s*-process nucleosynthesis models in AGB stars (e.g., Cseh et al. 2018, 2022), binary star evolution models (e.g., Escorza et al. 2020), and the mass-transfer mechanisms (e.g., Jorissen et al. 1998, 2016).

1.1. Barium dwarf stars

In addition to explaining the origins of the Ba/CH giants, the mass transfer scenario also predicts the existence of less evolved analogue stars exhibiting in their envelopes the Ba II syndrome observed in the classical giants. Indeed, the discovery of the so-called “CH *sub-giant* stars” (Bond 1974; Luck & Bond 1991, 1982) and the F/G-type main-sequence Ba *dwarf* stars (Tomkin et al. 1989; North et al. 1994), thought to be linked to the classical giants (see, e.g., Escorza et al. 2020), provided observational evidence in this sense.

Despite their nomenclatures, Ba dwarfs and CH subgiants exhibit many similarities. They share the same region in the HR diagram (Escorza et al. 2017), and exhibit no clear distinction in the period-eccentricity diagram (Escorza et al. 2019; North et al. 2020). From a chemical point of view, studies based on high-resolution spectroscopy point to the chemical similarity between Ba dwarfs and CH subgiants (Pereira & Junqueira 2003; Pereira 2005; Allen & Barbuy 2006a). These systems are generally referred to as Ba dwarfs and, just like the classical giants, also help us to trace back their former TP-AGB polluters, figuring as powerful tracers of the *s*-process nucleosynthesis.

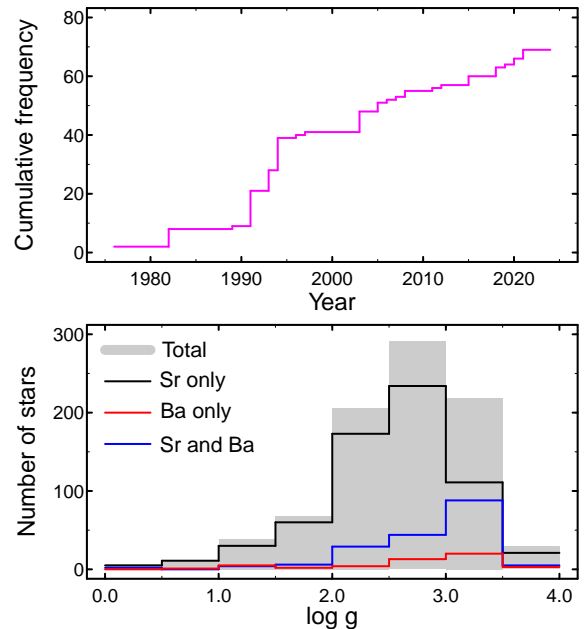


Figure 1. *Upper panel:* Temporal evolution of the cumulative frequency of Ba dwarf stars confirmed from detailed chemical analyses. *Bottom panel:* Distribution of the 895 *s*-process-rich candidates (grey) reported by Norfolk et al. (2019), identifying the sub-sample labeled as Sr only (black), Ba only (red), and Sr and Ba (blue). Stars with $\log g \geq 3.5$ represent only $\sim 0.3\%$ of the total number of the candidates.

However, Ba dwarfs turned out to be rare objects, calling into question whether they are the progenitors of the Ba/CH giants (e.g. Luck & Bond 1991). In light of the mass transfer hypothesis, the former are expected to be as common as the latter (Frantsman 1992; Han et al. 1995). A search of the literature reveals that the current sample of Ba dwarfs, confirmed from detailed chemical analyses, comprises only 69 stars. This is a relatively small number, compared to the current sample of Ba giants studied from high-resolution spectroscopy; for example, de Castro et al. (2016) reported an analysis of 169 Ba giants.

Moreover, as illustrated in the upper panel of Figure 1, the number of Ba dwarfs grown up very slowly over the years. In that plot, we show the temporal evolution of the cumulative frequency of these stars, starting from the first quantitative abundance analysis reported in the literature (Snedden & Bond 1976). In recent years, Ba dwarfs has been found in the studies of Kong et al. (2018), Purandardas et al. (2019), Shejeelammal et al. (2020), Liu et al. (2021), and Karinkuzhi et al. (2021). We refer the reader to Kong et al. (2018, and references therein) for a complete list until that year.

Recently, based on the Large Sky Area Multi-Object Fibre Spectroscopic Telescope (LAMOST) data along

with machine learning techniques, [Norfolk et al. \(2019\)](#) were able to select a sample of 895 *s*-process-rich candidates, using absorption features of Ba II and Sr II in their spectra. These stars were classified into three groups: those with only Ba enhancement (Ba only), only Sr enhancement (Sr only), and both Ba and Sr enhancements (Ba and Sr). However, the Ba only index turned out to be more reliable proxy for identifying potential Ba star candidates (see [Karinkuzhi et al. 2021](#); [Guo et al. 2023](#)). We have found 29 stars with superficial gravities such that $\log g \geq 3.5$ in the sample of [Norfolk et al.](#); among them, only 3 stars are marked as Ba only, according to the algorithm employed by [Norfolk et al.](#) This represents a very low frequency of occurrence (only $\sim 0.3\%$). In the bottom panel of Figure 1, we show the distribution of the sample analyzed by [Norfolk et al.](#) In other words, the task of finding Ba dwarfs is not easy, which reinforces the need of identifying new candidates and exploring their chemical patterns.

In the present work, we conduct a high-resolution spectroscopic analysis of two potential Ba dwarf candidates, HD 15096 and HD 37792. In addition to them, we have also include in our analysis the star HD 141804, previously classified as CH subgiants by [Luck & Bond \(1991\)](#), and a well-studied Ba dwarf (HD 207585). In the following, we describe in Section 2 the criteria adopted in selection of the targets, as well as the details of the observation and data acquisition; in Section 3, we give details of the spectroscopic analysis applied to the four stars; in Section 4, we describe the procedure to derive the elemental abundances; in Section 5, we discuss the abundance results in the literature context. In Section 6, we compare the observed patterns for the neutron-capture elements with predictions from the *s*-process nucleosynthesis models. In Section 7, we carry out a kinematic study for the program stars. Concluding remarks are outlined in Section 8.

2. PROGRAM STARS AND OBSERVATIONS

[Fulbright \(2000\)](#) conducted a high-resolution spectroscopic analysis of 168 halo and disk stars, mainly dwarfs. Among them, we noticed that HD 15096 and HD 37792 stood out of the data set, showing relatively high barium abundances, with $[\text{Ba}/\text{Fe}]^1$ ratios of +0.96 and +1.29 dex, respectively. Such high values caught our attention to consider these two targets as chemically peculiar candidates. Additionally, we realized that the barium abundance of HD 15096 is also accompanied by simi-

lar values for the $[\text{Y}/\text{Fe}]$ and $[\text{Zr}/\text{Fe}]$ ratios. However, no other neutron-capture element abundance data were reported for HD 15096 and HD 37792 in the literature.

The stars HD 141804 and HD 207585, in turn, belong to Table 3 of [Luck & Bond \(1991\)](#). That table lists 15 *s*-process enhanced stars with surface gravities ($\log g$) ranging from 3.0 to ~ 4.0 , so labeled as CH subgiants. Later works realized that some of these stars have different $\log g$ values, which put them in other evolutionary stage. This is the case of the stars BD+09°2384, CPD−62°6195 (=CD−62°1346), HD 122202, HD 123585, and HD 207585. For BD+09°2384 and CPD−62°6195, [de Castro et al. \(2016\)](#) and [Pereira et al. \(2012\)](#) found $\log g < 3.0$, which evidenced the giant nature of these stars. For HD 122202, HD 123585, and HD 207585, investigations carried out by [North et al. \(1994\)](#), [Allen & Barbuy \(2006a\)](#), [Karinkuzhi & Goswami \(2015\)](#), and [Shejeelammal et al. \(2020\)](#) reported $\log g$ values greater than those reported by [Luck & Bond](#), thus evidencing the dwarf nature of these objects.

For HD 141804, there is no other analysis in addition to that performed by [Luck & Bond \(1991\)](#). For this target, we present here for the first time elemental abundances of nitrogen, oxygen, aluminum, strontium, samarium, europium, and lead, as well as estimates of neutron exposure and a kinematic analysis. For HD 207585, on the other side, [Shejeelammal et al. \(2020\)](#) provided detailed elemental abundances and recognized the Ba dwarf nature of this object. However, as we will demonstrate later, we have found significant differences regarding the nitrogen and oxygen abundances reported by these authors. Additionally, we derive for the first time strontium abundances and estimated the neutron exposure level for HD 207585.

The high-resolution spectra of the program stars were acquired using the Fiber-fed Extended Range Optical Spectrograph (FEROS; [Kaufer et al. 1999](#)), installed at the 2.2 m Max Planck Gesellschaft (MPG)/European Southern Observatory (ESO) Telescope in La Silla, Chile. The observational missions were carried out between 2008 October and 2016 March. FEROS covers the spectral region between 3 500 and 9 200 Å with a resolving power $R = \lambda/\Delta\lambda \approx 48\,000$. In order to achieve a typical signal-noise ratio $S/N \approx 150\text{--}200$, the exposure time ranges from 600 to 1 200 s. We have used the FEROS Data Reduction System pipeline to reduce the observed spectra. General information about our targets are presented in Table 1, where we provided their positions, proper motions and parallaxes ([Gaia Collaboration 2020](#)), V and B magnitudes ([Zacharias et al.](#)

¹ Throughout this paper, we use the standard spectroscopic notation, $[\text{A}/\text{B}] = \log(N_{\text{A}}/N_{\text{B}})_{\star} - \log(N_{\text{A}}/N_{\text{B}})_{\odot}$, and the definition $\log \epsilon(\text{A}) = \log(N_{\text{A}}/N_{\text{H}}) + 12$.

2004), observation dates, and corresponding exposure times.

3. ATMOSPHERIC AND PHYSICAL PARAMETERS

The atmospheric parameters, effective temperature (T_{eff}), $\log g$, microturbulent velocity (ξ), and metallicity ($[\text{Fe}/\text{H}]$), for the stars HD 15096, HD 37792, HD 141804, and HD 207585 were derived by applying the same procedure described, for example, in Roriz et al. (2017), Pereira et al. (2019), and Holanda et al. (2020, 2023). Firstly, we measured the equivalent widths (EW) of a set of Fe I and Fe II absorption lines, by fitting Gaussian profiles to them. For this assignment, we have used the task SPLIT of the IRAF (Image Reduction and Analysis Facility; Tody 1986). The atomic parameters of the Fe I and Fe II transitions, such as excitation potential (χ) and $\log gf$ values, were taken from Lambert et al. (1996), i.e., the same line list consistently employed in the aforementioned references. The equivalent width measurements are listed in Table A1. In the task of deriving the atmospheric parameters, we implemented the version 2013 of the MOOG² spectral analysis code (Snedden 1973; Sneden et al. 2012). MOOG assumes the Local-Thermodynamic-Equilibrium (LTE) conditions and the plane-parallel atmosphere models. We have adopted the models computed by Kurucz (1993).

To find the effective temperature, we assumed the excitation equilibrium. Such a condition is verified when there is no trend between the iron abundances and the lower excitation potential of the measured Fe I lines, or when the slope of the linear fit is very close to zero. We derived the microturbulent velocity by constraining the Fe I lines until the iron abundance obtained from them shows no dependence with the reduced equivalent width ($\log \text{EW}/\lambda$). The surface gravity is computed by imposing the ionization equilibrium, i.e., when the Fe I and Fe II abundances are equal at the fixed T_{eff} .

The errors associated with temperatures were estimated considering the uncertainty in the value of the slope of the linear fit for Fe I abundances versus χ . On the other hand, the errors associated with microturbulent velocities were estimated from the uncertainty in the slope of the linear fit for the same Fe I abundances versus $\log \text{EW}/\lambda$. The errors in surface gravities were estimated by changing the $\log g$ value until the difference in the average abundances of Fe I and Fe II is equal to the standard deviation of the $[\text{Fe I}/\text{H}]$ mean. The final metallicity was normalized to the solar iron abun-

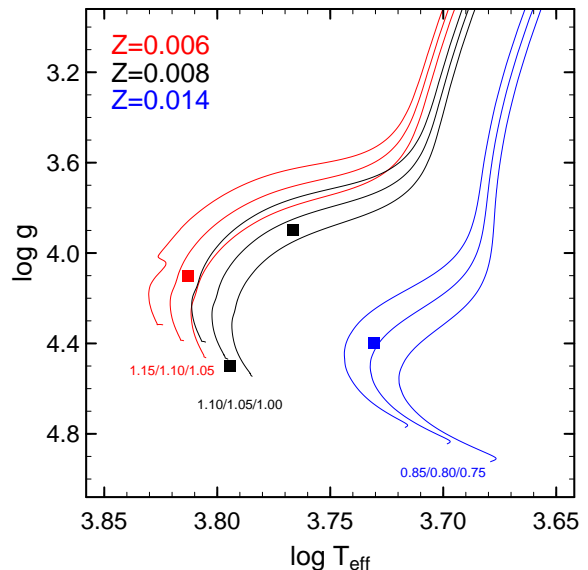


Figure 2. Position of the stars HD 15096 (blue), HD 37792 (red), HD 141804 (black), and HD 207585 (black) in the $\log T_{\text{eff}}$ versus $\log g$ diagram. Evolutionary tracks from Bressan et al. (2012), for $Z=0.006$, 0.008 , and 0.014 , are also shown; the numbers correspond to stellar masses (in solar unit, M_{\odot}).

dance recommendation of Grevesse & Sauval (1998), $\log \epsilon(\text{Fe}) = 7.50$ dex.

Table 2 presents the atmospheric parameters derived in this work and their respective uncertainties, along with data compiled from the literature. In general, we found a good agreement between our results and those reported in previous studies. Furthermore, Table 2 also lists the $\log g$ values derived from GAIA’s parallaxes (Gaia Collaboration 2020); these data corroborate the consistency of our results. In particular, for HD 141804, we derived $\log g = 4.50$, whereas Luck & Bond (1991) reported $\log g = 3.50$, which leads us to conclude that HD 141804 is, in fact, a dwarf star. Regarding HD 207585, we remark the close agreement between the atmospheric parameters derived in this work with those reported recently by Shejeelammal et al. (2020). It is also worth noting that these $\log g$ values are slightly larger than the value derived by Luck & Bond.

To estimate the masses and ages of our targets, we have used the PARSEC (PAдова and TRIeste Stellar Evolution Code; Bressan et al. 2012) evolutionary tracks and a Bayesian estimation method (da Silva et al. 2006). This estimation has been performed through PARAM³, a helpful tool to determine the ba-

² Available at <https://www.as.utexas.edu/chris/moog.html>

³ Available online at <http://stev.oapd.inaf.it/cgi-bin/param1.3>

Table 1. General description of our sample.

Star	RA (h m s)	DEC (° ' ")	V (mag)	B (mag)	pmRA (mas yr ⁻¹)	pmDEC (mas yr ⁻¹)	Plx (mas)	Date Obs. (yyyy-mm-dd)	Exp. (s)
HD 15096	02 26 01.76	+05 46 46.35	7.930	8.745	+383.857	+162.084	34.1998	2016-09-25	600
HD 37792	05 40 17.43	-19 13 37.77	7.722	8.093	-127.539	-192.658	13.3559	2016-09-09	600
HD 141804	15 53 29.24	-54 09 30.50	9.038	9.582	-21.448	-66.878	11.3044	2016-03-13	900
HD 207585	21 50 34.71	-24 11 11.69	9.785	10.482	+14.390	-36.805	4.8441	2008-10-19	1 200

Table 2. Adopted atmospheric and physical parameters for HD 37792, HD 15096, HD 141804, and HD 207585, in comparison with values previously reported in the literature.

Star	T_{eff} (K)	$\log g$ (cm s ⁻²)	[Fe/H] (dex)	ξ (km s ⁻¹)	$\log g^{\text{GAIA}}$ (cm s ⁻²)	Mass (M_{\odot})	Reference
HD 15096	5380±30	4.40±0.10	-0.14±0.06	0.80±0.10	4.51±0.02	0.85±0.03	This Work
	5375	4.30	-0.20	0.80	—	—	Fulbright (2000)
	5119	4.39	-0.48	0.43	—	—	Gratton et al. (2003)
	5247	4.35	-0.41	—	—	—	Soubiran & Girard (2005)
HD 37792	6500±20	4.10±0.20	-0.55±0.09	1.50±0.10	4.09±0.03	1.07±0.04	This Work
	6500	4.10	-0.60	1.50	—	—	Fulbright (2000)
HD 141804	6230±50	4.50±0.10	-0.41±0.08	1.20±0.10	4.35±0.03	0.99±0.04	This Work
	6000	3.50	-0.41	1.70	—	—	Luck & Bond (1991)
HD 207585	5840±50	3.90±0.20	-0.34±0.08	1.10±0.10	3.84±0.03	1.10±0.04	This Work
	5400	3.50	-0.74	—	—	—	Smith & Lambert (1986)
	5400±300	3.30±0.30	-0.57±0.05	1.80±0.50	—	—	Luck & Bond (1991)
	5800±100	3.80±0.20	-0.38±0.12	1.00±0.20	—	—	Shejeelammal et al. (2020)

sic intrinsic parameters of stars, given from their photometric and spectroscopic data. Individual values for masses and their respective uncertainties are also listed in Table 2. Additionally, the ages (in Gyr) derived from that procedure are 6.177 ± 3.623 (HD 15096), 4.768 ± 0.556 (HD 37792), 4.241 ± 1.729 (HD 141804), and 5.858 ± 0.561 (HD 207585). The positions of these stars in the Kiel Diagram are shown in Figure 2, along with evolutionary tracks for metallicities $Z = 0.006$, 0.008 , and 0.014 . From this plot, we see that at least HD 207585 is in a post-main-sequence evolutionary stage.

Since effective temperatures, surface gravities, and stellar masses have been derived for the program stars, we can evaluate their luminosities from the relation:

$$\log \left(\frac{L_{\star}}{L_{\odot}} \right) = 4 \log T_{\text{eff}\star} - \log g_{\star} + \log \left(\frac{M_{\star}}{M_{\odot}} \right) - 10.61, \quad (1)$$

for which we adopted $T_{\text{eff}\odot} = 5777$ K and $\log g_{\odot} = 4.44$. By inserting the data provided in Table 2 into Equa-

tion (1), we found $\log(L_{\star}/L_{\odot}) = -0.16 \pm 0.10$, $+0.57 \pm 0.20$, $+0.06 \pm 0.10$, and $+0.60 \pm 0.20$, for HD 15096, HD 37792, HD 141804, and HD 207585, respectively.

We can also derive their luminosities based on parallaxes, from the relation:

$$\log \left(\frac{L_{\star}}{L_{\odot}} \right) = -2 \log \pi + 0.4(M_{\text{bol}\odot} - V + A_V - \text{BC} - 5), \quad (2)$$

where π is the parallax (in arcsec), $M_{\text{bol}\odot} = 4.740 \pm 0.024$ is the solar bolometric magnitude of Bessell et al. (1998), V is the visual magnitude, BC is the bolometric correction, and A_V is the interstellar extinction. The bolometric corrections were evaluated from the empirical calibrations provided by Alonso et al. (1995) for dwarf stars, whereas the A_V values were estimated from the empirical extinction law of Chen et al. (1998). From this procedure, we have estimated $\log(L_{\star}/L_{\odot}) = -0.31 \pm 0.04$, $+0.63 \pm 0.05$, $+0.28 \pm 0.06$, and $+0.65 \pm 0.05$, for HD 15096, HD 37792, HD 141804, and HD 207585, respectively.

3.1. Radial velocity data

As will be discussed in Section 5, the chemical peculiarities observed in our stars cannot be explained in light of the stellar evolution of an isolated star, but in the mass transfer framework. Hence, in this section, we discuss the binary status of our targets. According to SIMBAD database, they are all classified as spectroscopic binaries. Three of them, HD 15096, HD 141804, and HD 207585, have their orbital elements already determined, and made available in the ninth catalogue of spectroscopic binary orbits (the SB9⁴ database; Pourbaix et al. 2004). HD 15096, HD 141804, and HD 207585 exhibit circular orbits (i.e., $e \sim 0.0$) with orbital periods (in days) of $3\,600 \pm 41$, $2\,652 \pm 95$, and 672 ± 2 , respectively (Latham et al. 2002; Escorza et al. 2019). As binary systems, their chemical peculiarities are attributable to mass transfer. We have also derived their radial velocities, from the Doppler shift of the spectral lines. We obtained, in km s^{-1} , -5.625 ± 0.194 , $+10.133 \pm 0.440$, -55.301 ± 0.406 , and -55.891 ± 0.309 for HD 15096, HD 37792, HD 141804, and HD 207585, respectively.

4. ABUNDANCE ANALYSIS

Chemical abundances were derived for a set of 21 different elements, based on either equivalent width measurements or synthetic spectra computations of selected absorption lines. To carry out this task, we have used the drivers *abfind*, *blends*, and *synth* of MOOG. The final abundances are presented in Tables 3 and 4, and a comparison with literature values is provided in Table 5. Our abundance data are normalized to the solar value recommended by Grevesse & Sauval (1998).

Carbon abundances were determined from equivalent width measurements of some absorption atomic lines of C I and also by computing synthetic spectra of molecular band heads for the stars HD 15096, HD 141804, and HD 207585. For HD 37792, the warmer (6 500 K) star of the program, the carbon molecular features were present for carbon abundance determination. Therefore, carbon abundance for this object was estimated only based on the C I atomic lines present in its spectrum, as seen in Table 3. To synthesize the molecular carbon features observed in HD 15096, HD 141804, and HD 207585, we used the C₂ (0,0) band head of the Swan system $d^3\Pi_g - a^3\Pi_u$ at 5 165 Å, as performed in Roriz et al. (2017), and the C₂ (0,1) band head of the Swan system $d^3\Pi_g - a^3\Pi_u$ at 5 635 Å, as in Drake & Pereira (2008). Figure 3 shows the observed and synthetic spectra around the spectral

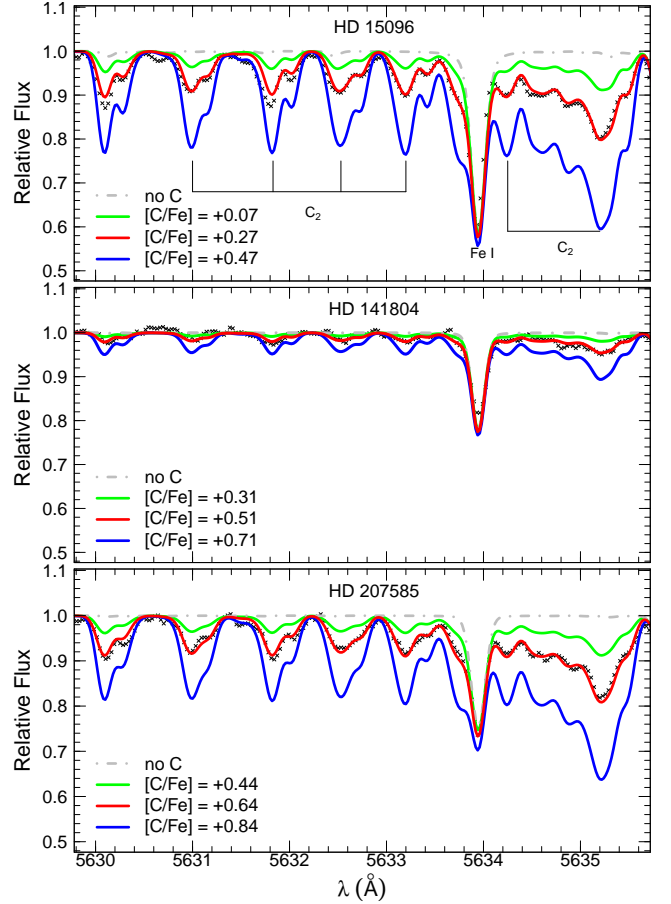


Figure 3. Observed (crosses) and synthetic (lines) spectra around the spectral region of the C₂ molecular band at 5 635 Å for the stars HD 15096, HD 141804, and HD 207585. The synthetic spectra were computed for different [C/Fe] values, as indicated in each panel. The gray lines are spectral synthesis without contribution of the C₂ molecule.

region of the C₂ molecular band at 5 635 Å, for these stars.

Nitrogen abundances were also obtained via spectral synthesis technique. For HD 15096, we used the ¹²CN molecular lines of the system A²Π – X²Σ in the 7 994–8 020 Å wavelength range, adopting the same linelist provided in Drake & Pereira (2008). For the stars HD 141804 and HD 207585, we used the B²Σ – X²Σ violet system band head at 3 883 Å, as done in Roriz et al. (2017), with the linelist provided by the Vienna Atomic Line Database (VALD; Ryabchikova et al. 2015). For HD 37792, however, we were not able to derive its nitrogen abundance. Additionally, the carbon isotopic ratios, ¹²C/¹³C, could not be measured in our program stars, as they are too hot to identify the ¹³CN lines. It is also worth mentioning that nitrogen abundances in Ba dwarfs are reported in the literature for a very limited number of stars (Reddy et al. 2003; Allen & Barbuy

⁴ Available on line at <https://sb9.astro.ulb.ac.be/>

Table 3. Elemental abundances derived for the stars HD 15096 and HD 37792. For guidance, solar photospheric abundances adopted in this work (Grevesse & Sauval 1998) are listed in the second column. Third and eighth columns provide the stellar abundances in the scale $\log \epsilon(\text{H}) = 12.0$; an asterisk is used to indicate abundances with non-LTE corrections. Abundances in the $[\text{X}/\text{H}]$ and $[\text{X}/\text{Fe}]$ notations are also shown. In columns 4 and 9, we provide the abundance dispersion (σ_{obs}) due to line-to-line scatter. These were evaluated when three or more transitions are considered, except for strontium and elements whose abundances were derived from spectral synthesis (syn), as explained in the text. For abundances based on equivalent width measurements, we provide information on the number of spectral lines used. At the end, we give the mean carbon abundance, considering the abundances derived from atomic absorption lines and the synthesis of molecular bands with the respective dispersion. In this case $n(\#)$ is the the number of the abundances obtained.

Species	$\log \epsilon_{\odot}$	HD 15096					HD 37792				
		$\log \epsilon$	σ_{obs}	$n(\#)$	$[\text{X}/\text{H}]$	$[\text{X}/\text{Fe}]$	$\log \epsilon$	σ_{obs}	$n(\#)$	$[\text{X}/\text{H}]$	$[\text{X}/\text{Fe}]$
C I	8.52	8.67	0.09	03	+0.15	+0.29	8.43	0.10	11	-0.09	+0.46
C (C ₂ 5 165)	8.52	8.70	0.02	syn	+0.18	+0.32	—	—	—	—	—
C (C ₂ 5 635)	8.52	8.65	0.03	syn	+0.13	+0.27	—	—	—	—	—
N	7.92	8.07	0.10	syn	+0.15	+0.29	—	—	—	—	—
O I	8.83	8.83	0.33	syn	0.00	+0.14	8.55*	0.04	03	-0.28	+0.27
Na I	6.33	6.18	0.06	04	-0.15	-0.01	5.97	0.05	04	-0.36	+0.19
Mg I	7.58	7.58	0.10	05	0.00	+0.14	7.18	0.10	07	-0.40	+0.15
Al I	6.47	6.24	0.05	06	-0.23	-0.09	—	—	—	—	—
Si I	7.55	7.51	0.04	05	-0.04	+0.10	7.17	0.07	05	-0.38	+0.17
Ca I	6.36	6.22	0.08	10	-0.14	0.00	5.93	0.09	15	-0.43	+0.12
Ti I	5.02	4.79	0.09	20	-0.23	-0.09	4.42	0.08	14	-0.60	-0.05
Cr I	5.67	5.44	0.06	05	-0.23	-0.09	5.02	0.07	08	-0.65	-0.10
Fe I	7.50	7.36	0.06	89	-0.14	—	6.95	0.09	74	-0.55	—
Fe II	7.50	7.35	0.05	14	-0.15	—	6.95	0.07	12	-0.55	—
Ni I	6.25	6.05	0.08	21	-0.20	-0.06	5.85	0.11	07	-0.40	+0.15
Sr I	2.97	3.70	0.04	01	+0.73	+0.87	3.04	0.07	01	+0.07	+0.62
Y II	2.24	3.07	0.07	05	+0.83	+0.97	2.54	0.09	06	+0.30	+0.85
Zr II	2.60	3.51	0.14	04	+0.91	+1.05	2.98	0.11	04	+0.38	+0.93
Ba II	2.13	3.13	0.06	syn	+1.00	+1.14	3.03	0.10	syn	+0.90	+1.45
La II	1.17	1.96	0.11	05	+0.79	+0.93	1.59	0.09	03	+0.42	+0.97
Ce II	1.58	2.47	0.10	07	+0.89	+1.03	2.05	0.08	06	+0.47	+1.02
Nd II	1.50	2.25	0.05	07	+0.75	+0.89	1.93	0.11	07	+0.43	+0.98
Sm II	1.01	1.68	0.03	04	+0.67	+0.81	1.78	—	02	+0.77	+1.32
Eu II	0.51	0.71	0.09	syn	+0.20	+0.34	—	—	—	—	—
Pb I	1.95	2.85	0.10	syn	+0.90	+1.04	<1.90	—	syn	< -0.05	< +0.50
C	8.52	8.67	0.03	03	+0.15	+0.29	—	—	—	—	—

2006a; Drake & Pereira 2007; Purandardas et al. 2019; Shejeelammal et al. 2020; Liu et al. 2021). Among them, many values are upper limits for the $[\text{N}/\text{Fe}]$ ratios.

Concerning oxygen abundances, we have used the $[\text{O I}]$ forbidden line at 6 300.3 Å for the star HD 15096, and adopted $\log gf = -9.72$ from Allende Prieto et al. (2001). For HD 37792, HD 141804, and HD 207585, oxygen abundances were evaluated from the equivalent width measurements of the oxygen infrared triplet around 7 774 Å. Taking into account the well known non-LTE effects in the oxygen infrared triplet lines, we performed non-LTE corrections for abundances derived

from the O I triplet lines. For this, we used yields of Amarsi et al. (2015), which are available by the INSPECT database, version 1.0 (<http://www.inspect-stars.com/>). After the non-LTE corrections, the $[\text{O}/\text{Fe}]$ ratios for HD 141804 and HD 207585 were lowered by 0.22 and 0.31 dex, respectively, while for HD 15096 the corrected $[\text{O}/\text{Fe}]$ ratio increased in 0.02 dex. The adopted values are marked with an asterisk in Tables 3 and 4.

For the light elements Na, Mg, Al, Si, Ca, and Ti, iron-group elements Cr and Ni, and the neutron-capture elements Sr, Y, Zr, La, Ce, Nd, and Sm, abundances were derived from equivalent width measurements of selected

Table 4. The same as in Table 3, for the stars HD 141804 and HD 207585.

Species	$\log \epsilon_{\odot}$	HD 141804					HD 207585				
		$\log \epsilon$	σ_{obs}	$n(\#)$	[X/H]	[X/Fe]	$\log \epsilon$	σ_{obs}	$n(\#)$	[X/H]	[X/Fe]
C I	8.52	8.85	0.08	09	+0.33	+0.74	8.97	0.09	09	+0.45	+0.79
C (C ₂ 5 165)	8.52	8.72	0.03	syn	+0.20	+0.61	8.72	0.03	syn	+0.20	+0.54
C (C ₂ 5 635)	8.52	8.62	0.10	syn	+0.10	+0.51	8.82	0.03	syn	+0.30	+0.64
N	7.92	7.62	0.03	syn	-0.30	+0.11	7.52	0.04	syn	-0.40	-0.06
O I	8.83	8.58*	0.04	03	-0.25	+0.16	8.55*	0.10	03	-0.28	+0.06
Na I	6.33	6.06	0.06	04	-0.27	+0.14	6.18	0.10	04	-0.15	+0.19
Mg I	7.58	7.29	0.12	04	-0.29	+0.12	7.33	0.06	03	-0.25	+0.09
Al I	6.47	5.96	0.07	03	-0.51	-0.10	5.96	0.07	04	-0.51	-0.17
Si I	7.55	7.32	0.04	03	-0.23	+0.18	7.39	0.07	03	-0.16	+0.18
Ca I	6.36	6.01	0.07	16	-0.35	+0.06	6.09	0.09	17	-0.27	+0.07
Ti I	5.02	4.54	0.06	16	-0.48	-0.07	4.56	0.08	18	-0.46	-0.12
Cr I	5.67	5.22	0.07	08	-0.45	-0.04	5.30	0.10	05	-0.37	-0.03
Fe I	7.50	7.09	0.08	64	-0.41	—	7.16	0.08	73	-0.34	—
Fe II	7.50	7.10	0.07	12	-0.40	—	7.16	0.08	11	-0.34	—
Ni I	6.25	5.92	0.08	10	-0.33	+0.08	5.96	0.09	09	-0.29	+0.05
Sr I	2.97	3.81	0.07	01	+0.84	+1.25	3.88	0.07	01	+0.91	+1.25
Y II	2.24	3.18	0.05	06	+0.94	+1.35	3.24	0.10	06	+1.00	+1.34
Zr II	2.60	3.67	0.11	07	+1.07	+1.48	3.78	0.11	06	+1.18	+1.52
Ba II	2.13	3.43	0.06	syn	+1.30	+1.71	3.53	0.02	syn	+1.40	+1.74
La II	1.17	2.29	0.05	05	+1.12	+1.53	2.21	0.09	05	+1.04	+1.38
Ce II	1.58	2.86	0.09	12	+1.28	+1.69	2.84	0.09	06	+1.26	+1.60
Nd II	1.50	2.68	0.08	14	+1.18	+1.59	2.61	0.06	10	+1.11	+1.45
Sm II	1.01	1.94	0.07	06	+0.93	+1.34	1.88	0.07	07	+0.87	+1.21
Eu II	0.51	0.88	0.05	syn	+0.37	+0.78	0.76	0.04	syn	+0.25	+0.59
Pb I	1.95	3.00	0.13	syn	+1.05	+1.46	2.96	0.10	syn	+1.01	+1.35
C	8.52	8.73	0.12	03	+0.21	+0.62	8.84	0.13	03	+0.32	+0.66

atomic lines sufficiently unblended to provide reliable abundances of such species. In Table A2 of Appendix, we provide the adopted lab data, such as wavelength, excitation potentials, and $\log gf$ values, of the atomic transitions used in our analysis, as well as the measured equivalent widths. For the element lanthanum, in particular, we have followed the same procedure employed by Roriz et al. (2021b). In other words, we measured the equivalent widths of the lanthanum lines and run driver *blends* of MOOG, which provides abundances from blended spectral lines, to take into account the hyperfine splitting (HFS) that strongly affect the transitions of this element.

Barium, europium, and lead abundances, on the other hand, were determined from synthetic spectrum analysis. For barium abundances, we used the Ba II line at 5 853.7 Å, and adopted its HFS data from McWilliam (1998). For europium, we considered the Eu II line at 6 645.1 Å, for which HFS components were taken from

Lawler et al. (2001b). Lead abundances were derived from the Pb I line at 4 057.8 Å. HFS and isotopic data for lead were taken from Van Eck et al. (2003).

4.1. Abundance uncertainties

In the task of deriving chemical abundances, two uncertainty sources should be taken into account: (i) the line parameters, as equivalent width measurements, oscillator strength values, continuum normalization, and line blending, which introduce random errors (σ_{ran}) in abundances, as well as (ii) the errors associated with stellar parameters of atmospheric models. For a generic element X, the total uncertainty in $\log \epsilon(X)$ can be evaluated according to the following equation:

Table 5. Comparison between elemental abundances derived in (1) this work, (2) [Fulbright \(2000\)](#), (3) [Luck & Bond \(1991\)](#), (4) [Shejeelammal et al. \(2020\)](#), and (5) [Masseron et al. \(2010\)](#).

Star	[C/Fe]	[N/Fe]	[O/Fe]	[Na/Fe]	[Mg/Fe]	[Al/Fe]	[Si/Fe]	[Ca/Fe]	[Ti/Fe]	[Cr/Fe]	Ref.
HD 15096	+0.29	+0.29	+0.14	-0.01	+0.14	-0.09	+0.10	0.00	-0.09	-0.09	1
	-	-	-	+0.04	+0.21	+0.19	+0.08	+0.09	+0.13	-0.01	2
HD 37792	+0.46	-	+0.27	+0.19	+0.15	-	+0.17	+0.17	-0.05	-0.10	1
	-	-	-	+0.13	+0.11	-	+0.31	+0.15	+0.33	-	2
HD 141804	+0.62	+0.11	+0.16	+0.14	+0.12	-0.10	+0.18	+0.06	-0.07	-0.04	1
	+0.24	-	-	+0.01	-0.08	-	+0.14	+0.15	+0.32	-0.03	3
HD 207585	+0.66	-0.06	+0.06	+0.19	+0.09	-0.17	+0.18	+0.07	-0.12	-0.03	1
	-	-	-	+0.25	+0.02	-	+0.28	+0.39	+0.01	+0.24	3
	+0.61	+0.75	+0.97	+0.25	+0.07	-	+0.12	+0.26	+0.01	+0.13	4
	+0.51	+0.12	+0.14	-	-0.03	-	-	-	-	-	5

Star	[Ni/Fe]	[Y/Fe]	[Zr/Fe]	[Ba/Fe]	[La/Fe]	[Ce/Fe]	[Nd/Fe]	[Sm/Fe]	[Eu/Fe]	[Pb/Fe]	Ref.
HD 15096	-0.06	+0.97	+1.05	+1.14	+0.93	+1.03	+0.89	+0.81	+0.34	+1.04	1
	0.00	+1.02	+1.00	+0.96	-	-	-	-	+0.30	-	2
HD 37792	+0.15	+0.85	+0.93	+1.45	+0.97	+1.02	+0.98	+1.32	-	+0.50	1
	+0.10	-	-	+1.29	-	-	-	-	-	-	2
HD 141804	+0.08	+1.35	+1.48	+1.71	+1.53	+1.69	+1.59	+1.34	+0.78	+1.46	1
	+0.02	+0.60	+1.48	+1.25	+1.18	+1.10	+0.95	-	-	-	3
HD 207585	+0.05	+1.34	+1.52	+1.74	+1.38	+1.60	+1.45	+1.21	+0.59	+1.35	1
	+0.08	+1.30	+1.02	-	+1.61	+0.85	+0.94	+1.06	-	-	2
	-0.01	+1.37	+1.20	+1.60	+1.70	+1.72	+1.62	+2.04	+0.28	-	3
	-	-	-	+1.23	+1.37	+1.41	-	-	+0.58	+1.30	4

$$\begin{aligned}
\sigma_{\log \epsilon(X)_*}^2 &= \sigma_{\text{ran}}^2 + \left(\frac{\partial \log \epsilon}{\partial T_{\text{eff}}} \right)^2 \sigma_{T_{\text{eff}}}^2 \\
&+ \left(\frac{\partial \log \epsilon}{\partial \log g} \right)^2 \sigma_{\log g}^2 + \left(\frac{\partial \log \epsilon}{\partial \xi} \right)^2 \sigma_{\xi}^2 \\
&+ \left(\frac{\partial \log \epsilon}{\partial [\text{Fe}/\text{H}]} \right)^2 \sigma_{[\text{Fe}/\text{H}]}^2 + \left(\frac{\partial \log \epsilon}{\partial W_{\lambda}} \right)^2 \sigma_{W_{\lambda}}^2.
\end{aligned} \tag{3}$$

To evaluate the partial derivatives of the above equation, we shifted the parameters T_{eff} , $\log g$, ξ , $[\text{Fe}/\text{H}]$, and W_{λ} in +30 K, +0.1 dex, +0.1 km s⁻¹, +0.1 dex, and +3 mÅ, respectively, which are typical uncertainties. Then, we computed the corresponding change introduced in the abundance when we vary one of the parameters, keeping the others fixed. For a resolution $R = 48\,000$ and a typical signal-to-noise ratio $S/N \sim 100 - 200$, the expected uncertainties in the equivalent widths are of the order of 2 – 3 mÅ, according to [de Strobel & Spite \(1988\)](#). The σ_{ran} term in equation (3) takes into account the line-to-line scatter in abundance. It is evaluated as the

ratio $\sigma_{\text{obs}}/\sqrt{n}$, where σ_{obs} is the standard deviation and n is the number of spectral lines considered in the abundance derivation. Thus, the uncertainty in the $[\text{X}/\text{Fe}]$ ratios is given by:

$$\sigma_{[\text{X}/\text{Fe}]}^2 = \sigma_{\text{X}}^2 + \sigma_{\text{Fe}}^2. \tag{4}$$

The partial derivatives in Equation (3) were evaluated for HD 15096, taken as a template star. Table 6 shows as the abundances for HD 15096 change in response to changes in T_{eff} , $\log g$, ξ , $[\text{Fe}/\text{H}]$, and W_{λ} ; these values were assumed for the other targets. On the other hand, σ_{ran} was computed for each object, when three or more lines are used to derive abundances, except for strontium and elements whose abundances were derived from spectral synthesis. For these particular cases, σ_{obs} is evaluated from three different positions of the continuum.

For CNO abundances, the uncertainties were evaluated similarly. By varying one of the parameters T_{eff} , $\log g$, and ξ , keeping the others two constant, we com-

puted the respective changes introduced in abundances of HD 15096. Additionally, since CNO abundances are not independent of each other, we also evaluated the variations introduced as a consequence of changes in $\log \epsilon(\text{C})$, $\log \epsilon(\text{N})$, and $\log \epsilon(\text{O})$ individually. The results for the CNO uncertainty estimates are presented in Table 7.

5. RESULTS AND DISCUSSION

5.1. Carbon, nitrogen, and oxygen

Elemental abundances of carbon, nitrogen, and oxygen are sensitive indexes to stellar evolution stages, as well as the mixing events that take place within the stars and alter the chemical composition of their atmospheres. According to stellar evolution models, when a star becomes a giant, the nuclear material previously exposed to CN-cycle is brought to the stellar surface, as a result of convective motions, known as first dredge-up (FDU), changing the initial abundance pattern of the star. As an outcome of FDU, carbon is depleted and nitrogen is increased on the stellar surface, while the oxygen content remains unchanged. Unlike the classical Ba/CH stars, Ba dwarfs did not experience the FDU. Consequently, the *s*-processed material received from their companions is unmixed with the nuclear material internally processed in the star. This is particularly useful for studying carbon and nitrogen, whose abundances should reflect the added material.

In Figure 4, we show the $[\text{C}, \text{N}, \text{O}/\text{Fe}]$ ratios observed for HD 15096, HD 37792, HD 141804, and HD 207585 as function of metallicity. We have also added in this figure data compiled from different sources of the literature for dwarf and giant normal stars, classical Ba giants, and Ba dwarf stars (i.e., with $\log g \geq 3.5$). The program stars exhibit moderate levels of carbon enhancements, with $[\text{C}/\text{Fe}]$ ratios ranging from $\sim +0.30$ to $\sim +0.70$ dex, consistent with values already reported in the literature for Ba dwarfs of same metallicity.

Regarding nitrogen abundances in Ba dwarfs, the scarcity of data in the literature is noteworthy. Among the reported data, most of them are upper limits (see Allen & Barbuy 2006a), and are not plotted in Figure 4. It is remarked that Ba stars present generally a scatter larger than the observed in normal giant and dwarf stars, and some of them exhibit high levels of N abundances. It is known that massive ($\gtrsim 4.0 M_{\odot}$) TP-AGB stars are able to produce high amounts of nitrogen through the Hot Bottom Burning (HBB) phenomenon (Boothroyd et al. 1995), when the convective envelope of the AGB star deepens its base into the H-burning shell. In principle, this mechanism could account the nitrogen excess observed in some Ba stars, however, the patterns

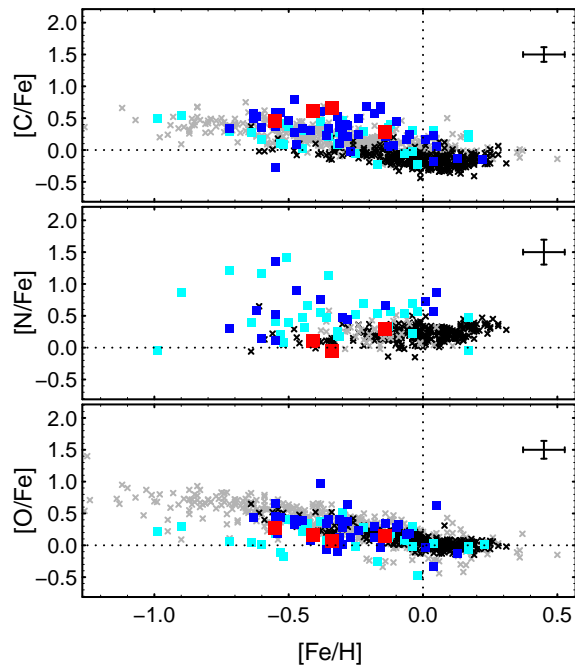


Figure 4. Abundance ratios for the elements carbon, nitrogen, and oxygen. The observed $[\text{C}, \text{N}, \text{O}/\text{Fe}]$ ratios for the program stars (red squares) are plotted as a function of metallicity. Typical error bars are shown in the top of the panels. Data for field dwarf stars (gray crosses), field giant stars (black crosses), Ba giant stars (cyan squares), and Ba dwarf/CH subgiant stars (blue squares), collected from different literature sources, are also plotted. Data for field giant stars were taken from Luck & Heiter (2007); data for field dwarf stars were taken from Reddy et al. (2003), Reddy et al. (2006), and Luck & Heiter (2006); data for Ba giant stars were taken from Allen & Barbuy (2006a), de Castro et al. (2016), Karinkuzhi et al. (2018b), Shejeelammal et al. (2020), and Roriz et al. (2021b); data for Ba dwarfs/CH subgiant stars were taken from Smith et al. (1993), Edvardsson et al. (1993), North et al. (1994), Porto de Mello & da Silva (1997), Reddy et al. (2003), Pereira & Junqueira (2003), Pereira (2005), Allen & Barbuy (2006a), Pereira & Drake (2011), Karinkuzhi & Goswami (2015), Kong et al. (2018), Purandardas et al. (2019), Shejeelammal et al. (2020), Liu et al. (2021), and Karinkuzhi et al. (2021).

observed for heavy elements in Ba stars evidence the low-mass ($\lesssim 3.0 M_{\odot}$) nature of the polluting AGB stars (e.g., Cseh et al. 2018; Karinkuzhi et al. 2018b; Shejeelammal et al. 2020; Roriz et al. 2021a,b; Cseh et al. 2022).

For HD 15096, HD 141804, and HD 207585, we have derived $[\text{N}/\text{Fe}] = +0.29$, $+0.11$, and -0.06 dex, respectively. These values are commonly found in normal stars, as seen in the middle panel of Figure 9. This in turn could indicate inefficiencies in the CN-cycle and/or FDU of the ancient polluting stars, when they became giants. For HD 37792, our warmest (6 500 K)

Table 6. Abundance uncertainties for HD 15096, taken as a template star. Second column gives the random errors, given by $\sigma_{\text{ran}} = \sigma_{\text{obs}}/\sqrt{n}$, where n is the number of absorption lines used for the abundance determination. Columns from 3 to 7 show variations in the abundances introduced by changes in T_{eff} , $\log g$, ξ , $[\text{Fe}/\text{H}]$, and equivalent width measurements (W_λ), respectively. By combining quadratically the terms from the 2nd to 7th, we estimate the total uncertainties, listed in column 8. The last column provides the abundance dispersion in abundance due to line-to-line scatter, previously shown in Table 3.

Species	σ_{ran}	ΔT_{eff} (+30 K)	$\Delta \log g$ (+0.1 dex)	$\Delta \xi$ (+0.1 km s ⁻¹)	$\Delta [\text{Fe}/\text{H}]$ (-0.1 dex)	ΔW_λ (+3 mÅ)	$\sqrt{\sum \sigma^2}$	σ_{obs}
C I	0.05	-0.02	+0.01	0.00	0.00	+0.08	0.10	0.09 (03)
Na I	0.03	+0.02	-0.02	-0.01	-0.01	+0.04	0.06	0.06 (04)
Mg I	0.04	+0.02	-0.01	-0.01	-0.01	+0.04	0.06	0.10 (05)
Al I	0.02	+0.02	-0.01	0.00	0.00	+0.05	0.06	0.05 (06)
Si I	0.02	-0.01	0.00	-0.01	-0.02	+0.05	0.06	0.04 (05)
Ca I	0.03	+0.03	-0.02	-0.02	-0.01	+0.05	0.07	0.08 (10)
Ti I	0.03	+0.04	0.00	-0.02	0.00	+0.07	0.09	0.09 (20)
Cr I	0.03	+0.04	-0.01	-0.03	-0.01	+0.06	0.08	0.06 (05)
Fe I	0.01	+0.01	-0.01	-0.03	-0.02	+0.06	0.07	0.06 (89)
Fe II	0.01	-0.02	+0.03	-0.02	-0.03	+0.08	0.10	0.05 (14)
Ni I	0.02	+0.01	+0.01	-0.02	-0.02	+0.07	0.08	0.08 (21)
Sr I	0.02	+0.04	-0.03	-0.03	-0.03	+0.04	0.08	0.04 (01)
Y II	0.03	+0.01	+0.02	-0.04	-0.03	+0.07	0.09	0.07 (05)
Zr II	0.07	0.00	+0.03	-0.04	-0.03	+0.09	0.13	0.14 (04)
Ba II	0.03	0.00	0.00	-0.10	-0.10	—	0.14	0.06 (syn)
La II	0.05	-0.01	+0.02	-0.01	-0.05	+0.07	0.10	0.11 (05)
Ce II	0.04	+0.01	+0.04	-0.03	-0.03	+0.10	0.12	0.10 (07)
Nd II	0.02	+0.01	+0.04	-0.02	-0.04	+0.11	0.13	0.05 (07)
Sm II	0.02	+0.01	+0.04	-0.02	-0.03	+0.11	0.12	0.03 (04)
Eu II	0.05	-0.05	0.00	0.00	-0.05	—	0.09	0.09 (syn)
Pb I	0.06	0.00	0.00	-0.10	-0.10	—	0.15	0.10 (syn)

Table 7. Abundance uncertainties of carbon, nitrogen, and oxygen for the star HD 15096.

Species	ΔT_{eff} (+30 K)	$\Delta \log g$ (+0.1 dex)	$\Delta \xi$ (+0.1 km s ⁻¹)	$\Delta \log (\text{C})$ (+0.20 dex)	$\Delta \log (\text{N})$ (+0.20 dex)	$\Delta \log (\text{O})$ (+0.20 dex)	$\sqrt{\sum \sigma^2}$
C	-0.01	+0.02	-0.01	—	0.00	+0.07	0.07
N	0.00	0.00	-0.02	-0.20	—	-0.14	0.24
O	0.00	+0.05	+0.05	-0.02	0.00	—	0.07

star, N abundance could not be determined. As we mentioned in Section 2, HD 207585 is a common star with the sample of Shejeelammal et al. (2020), who reported $[\text{N}/\text{Fe}] = +0.75$ dex (see Table 5), while we have found a significantly lower value ($[\text{N}/\text{Fe}] = -0.06$ dex). For the same object, Masseron et al. (2010) reported $[\text{N}/\text{Fe}] = +0.12$ dex. Similar disagreement concerns to oxygen abundances of HD 207585. In this work, we found $[\text{N}/\text{Fe}] = +0.06$ dex and Masseron et al. (2010) $[\text{N}/\text{Fe}] = +0.14$ dex, while Shejeelammal et al. reported a much higher value, $[\text{O}/\text{Fe}] = +0.97$ dex.

For oxygen, the third panel of Figure 4 shows that our stars follow the Galactic trend, as expected. Addition-

ally, we have derived their respective C/O ratios, which are commonly used to constraint Ba stars (C/O < 1; Barbuy et al. 1992; Allen & Barbuy 2006a; Pereira & Drake 2009; Karinkuzhi et al. 2018a,b; Roriz et al. 2023) and CH stars (C/O > 1; Pereira & Drake 2009; Pereira et al. 2012; Goswami et al. 2016; Purandardas et al. 2019). For HD 15096, HD 37792, HD 141804, and HD 207585, we found C/O = 0.69, 0.76, 1.41, and 1.95, respectively.

Considering the CNO abundance data, we can infer that carbon is actually the main responsible for the CNO excess observed in HD 15096, HD 141804, and HD 207585. This is also seen from their C+N combined

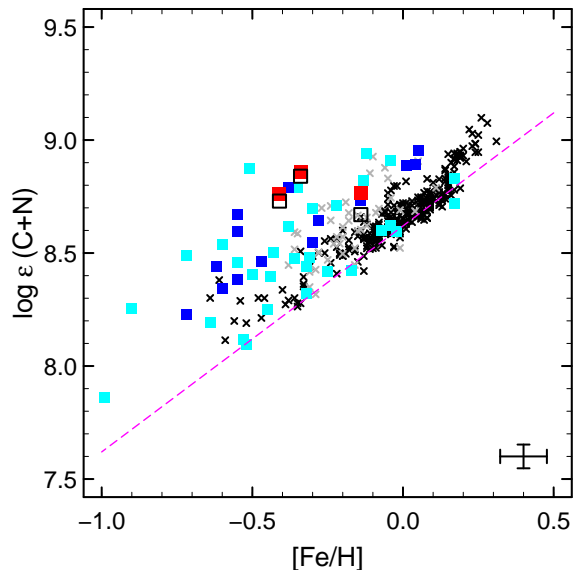


Figure 5. Combined carbon plus nitrogen abundances in the notation $\log \epsilon(\text{C} + \text{N})$ observed in HD 15096, HD 141804, and HD 207585 as a function of the metallicity. A typical error bar is also shown. The symbols have the same meaning as in Figure 4. To illustrate the role of carbon in the CNO excess in our stars, we show the respective logarithmic carbon abundances in empty black squares. The magenta dashed line shows the initial CN abundance for a given metallicity.

abundances, for which we have $\log \epsilon(\text{C} + \text{N}) = 8.76, 8.76,$ and 8.86 , respectively. In Figure 5, we compare the observed values of $\log \epsilon(\text{C} + \text{N})$ with those found in Ba dwarfs, Ba giants, and normal stars. It is notable that Ba stars present in this plane a scatter greater than the observed in normal field stars. Our stars lie close to other Ba dwarfs, which exhibit values systematically larger than those typically found in Ba giants. In conclusion, we see that the atmospheres of our stars were, indeed, contaminated by material previously exposed to He-burning shell.

5.2. Elements from sodium to nickel

We extracted chemical abundances for Na, α -elements (Mg, Al, Si, Ca, and Ti), and iron-group (Cr and Ni) elements. Nucleosynthesis computations performed by Wosley & Weaver (1995) predict that the elements sodium, magnesium, aluminum, silicon, calcium, and titanium in the Galaxy are mainly produced in hydrostatic burning environments of stars with initial masses of $10 - 40 M_{\odot}$, as well as in supernova events. Sodium, magnesium, and aluminum are by-products of carbon burning, while most silicon, calcium, and titanium are produced from oxygen burning. Magnesium nucleosynthesis has also a contribution from hydrostatic neon burning. Type II supernova events are able to synthe-

size silicon and calcium, whereas the elements titanium, iron, chromium, and nickel, belonging to iron-group, are mainly produced from Type Ia supernovae. Therefore, Ba stars are expected to follow the Galactic trend for these elements. According to data in Tables 3 and 4, the $[\text{X}/\text{Fe}]$ ratios for elements from Na to Ni are close to zero, similar to values observed in normal field stars.

In particular, for the odd-Z element Na, the $[\text{Na}/\text{Fe}]$ ratios observed in field stars of the Galaxy show no trend for $[\text{Fe}/\text{H}] \gtrsim -1.0$ dex (e.g. Luck & Heiter 2006, 2007). For the studied stars, we found the $[\text{Na}/\text{Fe}]$ ratios ranging from -0.03 to $+0.19$ dex, consistent with values reported for Ba dwarfs (e.g. Allen & Barbuy 2006a). Na can be produced through the NeNa-chain, during the H-burning in the convective core of main-sequence stars with mass $M \gtrsim 1.5 M_{\odot}$. Then, when the star becomes a giant, FDU brings Na to the stellar surface, along with the by-products of CNO-cycle. However, since our targets did not reach the giant-branch stage of their evolution, their internally processed nuclear material was not dredged yet, so that our targets behave as normal stars. Works in the literature (Antipova et al. 2004; de Castro et al. 2016; Karinkuzhi et al. 2018b; Shejeelammal et al. 2020) reported $[\text{Na}/\text{Fe}] \gtrsim +0.4$ dex for Ba giants, and de Castro et al. (2016) observed an anti-correlation between $[\text{Na}/\text{Fe}]$ and $\log g$ for the stars of their sample (see their Figure 20).

Na production is also associated with nucleosynthesis in AGB stars. Models predict that AGB stars are able to produce ^{23}Na from Ne isotopes, through the NeNa-chain of proton capture, via $^{22}\text{Ne}(p,\gamma)^{23}\text{Na}$ reaction, where the ^{22}Ne was previously synthesized in the He-burning shell, from the $^{14}\text{N}(\alpha,\gamma)^{18}\text{F}(\beta^+)^{18}\text{O}(\alpha,\gamma)^{22}\text{Ne}$ reaction sequences (e.g., Mowlavi 1999; Karakas & Lattanzio 2014). The processed material is mixed and brought to the AGB atmosphere, via Third Dredge-Up (TDU), and then is subsequently transferred to the observed Ba star. However no Na enhancement is observed in our stars.

5.3. Neutron-capture elements

Elements beyond the iron-peak ($Z > 30$) are primarily synthesized throughout neutron-captures on seed nuclei, the s -process and the so-called r - (*rapid*) process, depending on the time involved between neutron captures and β decays. While the s -process takes place within TP-AGB stars, the exact astrophysical site(s) of the r -process is(are) a matter of debate, although supernovae events and neutron star mergers figure among the most promising scenarios (see the review of Cowan et al. 2021). As far as heavy elements are concerned, we have derived for our sample elemental abundances for Sr, Y,

Table 8. Contribution (%) of the s -process to the solar-system material as provided by Arlandini et al. (1999, A99) and Bisterzo et al. (2014, B14).

Species	A99	B14
Sr	85	69
Y	92	72
Zr	83	66
Ba	81	85
La	62	76
Ce	77	84
Nd	56	58
Sm	29	31
Eu	6	6
Pb	46	87

Zr, Ba, La, Ce, Nd, Sm, Eu, and Pb. As anticipated in Introduction, the chemical patterns of heavy elements observed in Ba stars help us to trace back their former polluter TP-AGB stars.

Table 8 lists the s -process contribution to the Solar system material, where we can see a high contribution of the s -process in nucleosynthesis of the elements Sr, Y, Zr, Ba, La, Ce, and Nd. Indeed, they are found very abundant in our targets, with $[X/Fe]$ ratios $\gtrsim +1.00$ dex, evidencing the strong s -rich nature of these objects, while normal field stars show $[X/Fe]$ close to zero. Lead abundances are also enhanced in HD 15096, HD 141804, and HD 207585, with $[Pb/Fe] = +1.04, +1.46,$ and $+1.35$ dex, respectively. For HD 37792, we were able to report only the upper limit $[Pb/Fe] < +0.50$ dex. Data on lead abundances, however, are very scarce in the literature. For the element samarium, which has a low s -process contribution (see Table 8), we also found excesses in our stars ($+0.80 < [Sm/Fe] < +1.35$). These high levels are not effects of the Galactic chemical evolution, and are found in Ba giants and other Ba dwarfs (Allen & Barbuy 2006a). Europium, a representative element of the r -process, shows slightly enhanced abundances in our stars, with $[Eu/Fe]$ values of $+0.34, +0.78,$ and $+0.59$ dex for HD 15096, HD 141804, and HD 207585, respectively. For HD 37792, europium abundance could not be derived, since the diagnostic spectral line was faintly detectable in its spectrum.

In Figure 6, we located our stars in the $[La/Fe]$ versus $[Eu/Fe]$ diagram, along with data available for other Ba dwarfs. We also added to this plot data for Ba giants and CEMP (Carbon-Enhanced Metal-Poor) stars (Beers & Christlieb 2005; Masseron et al. 2010). Since La and Eu are representative elements of the s - and r -processes, respectively, this diagram is able to split the

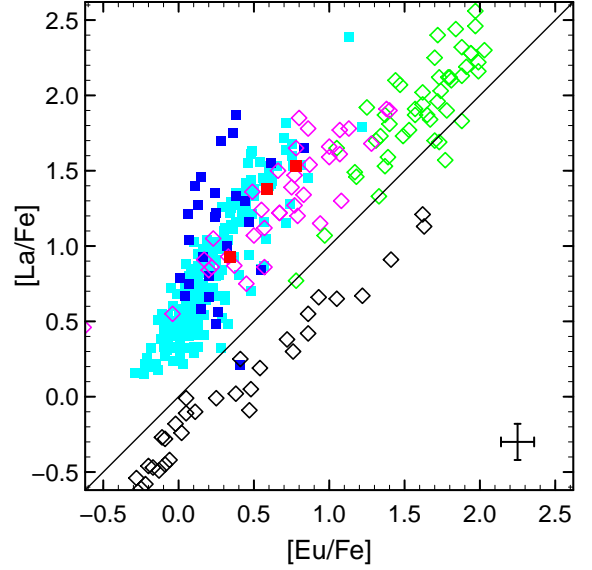


Figure 6. Program stars in the $[La/Fe]$ versus $[Eu/Fe]$ plane, along with data for other Ba dwarfs and Ba giants. Symbols and the literature references are the same listed in the caption of Figure 4. Diamonds are data for CEMP- r (black), CEMP- s (magenta), and CEMP- r/s (green), taken from Masseron et al. (2010) and Karinkuzhi et al. (2021).

data according the neutron-capture levels of enrichment observed in the stars. As demonstrated in that figure, our stars share the same portion (the s -rich side) where other Ba dwarfs, Ba giants, and the CEMP- s lie.

5.3.1. The s -process indexes

The $[hs/ls]$ ratio is an intrinsic s -process index, widely used to probe the neutron exposures of the s -process (e.g., Luck & Bond 1991; Busso et al. 2001). This ratio is defined as the difference $[hs/Fe] - [ls/Fe]$, where $[hs/Fe]$ and $[ls/Fe]$ are the averaged abundances of the elements belonging to the second (Ba, La, Ce, Nd) and first (Sr, Y, Zr) s -process peaks. High neutron exposures push nucleosynthesis of the second peak elements, instead elements of the first peak, so that $[hs/ls] > 0$ is expected. HD 15096, HD 37792, HD 141804, and HD 207585, show $[hs/ls] = +0.04, +0.31, +0.27,$ and $+0.17$ dex, respectively. As shown in the upper panel of Figure 7, these values are consistent those reported in the literature for Ba stars. The $[Pb/hs]$ ratio is useful to probe the nucleosynthesis among the third (Pb) and second peaks. We found $[Pb/hs] = +0.04, -0.61, -0.17,$ and -0.19 dex for HD 15096, HD 37792, HD 141804, and HD 207585, respectively. However, the literature lacks for lead abundance data (see middle panel of Figure 7). Considering the $[hs/ls]$ and $[Pb/hs]$ ratios, we conclude that the neutron exposures favored the nucleosynthesis of the second peak elements.

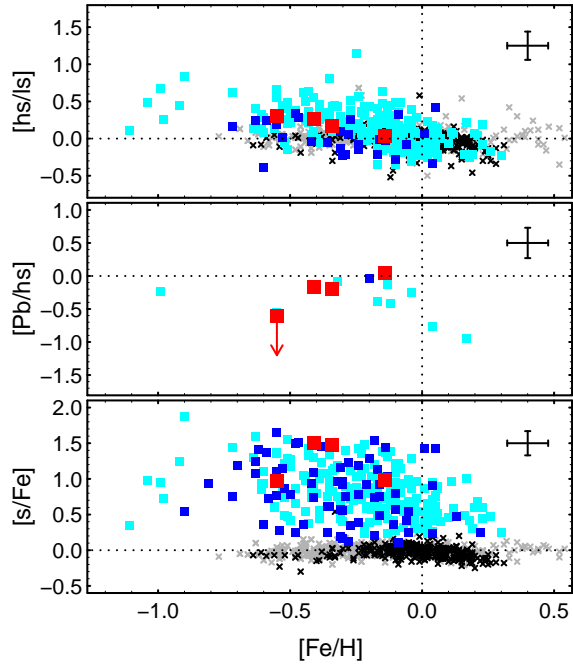


Figure 7. Indexes of the s -process. *Upper, middle, and bottom* panels show respectively the $[hs/ls]$, $[Pb/hs]$, and $[s/Fe]$ ratios as function of metallicity. Symbols and the literature references are the same listed in the caption of Figure 4. Typical error bars for our data are also showed in the panels.

We also computed the $[s/Fe]$ index, given by the s -process average abundances from elemental abundances for Sr, Y, Zr, Ba, La, Ce, Nd, and Pb, yielding $[s/Fe] = +0.99, +0.92, +1.10,$ and $+1.45$ dex for HD 15096, HD 37792, HD 141804, and HD 207585, respectively. Normal field stars typically show $[s/Fe] \sim 0$, whereas Ba stars exhibit $[s/Fe]$ ratios increasing for lower metallicity regimes (see the bottom panel of Figure 7), a feature of the s -process (e.g. Busso et al. 2001). In their study on Ba giant stars, de Castro et al. (2016) assumed $[s/Fe] > +0.25$ dex as a criterion to classify a star as Ba star, and ours stars satisfy this condition.

5.3.2. Mean neutron exposures

To infer quantitatively on the neutron exposure levels to which the s -processed material observed in our targets was subjected, we have used the classical analysis of the main s -process component (Kaeppler et al. 1990; Käppeler et al. 2011) to estimate the mean neutron exposures (τ_0). This approach consists of the so-called σN_s curve, which show the behavior of the product between the neutron-capture cross-sections (σ) and the abundances of the main s -process component (N_s), traditionally expressed in the scale $\log \epsilon(\text{Si}) = 6.0$. The σN_s curve is written in terms of τ_0 and G , which are free parameters to fit the observations, where G is the

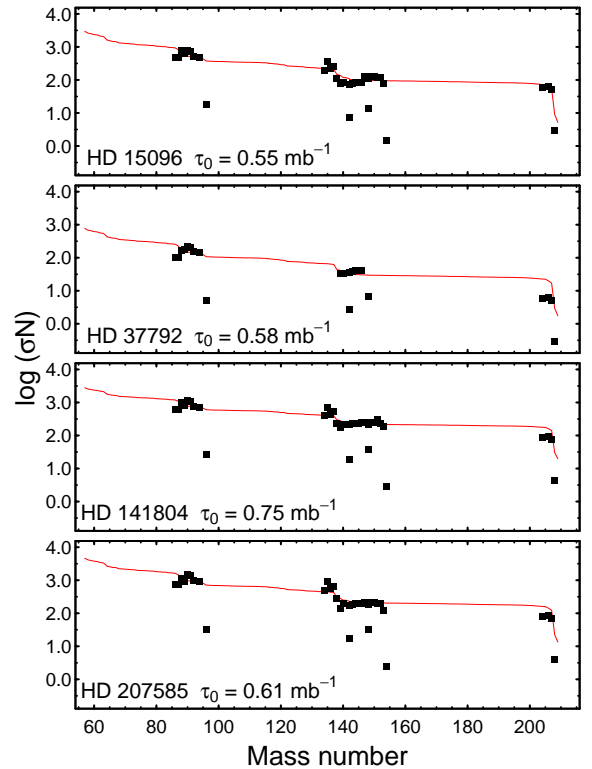


Figure 8. Fitting of theoretical σN_s curves (red lines) and observed σN_s values (black squares). The data are plotted in logarithmic scale; σ is expressed in mb and N_s in the scale $\log \epsilon(\text{Si}) = 6.0$. The estimated neutron exposures are shown in the bottom of panels.

fraction of ^{56}Fe used as seed of the s -process. G has the effect of shifting the curve, while τ_0 changes the shape of the σN_s curve. An interesting feature of the classical approach is that it successfully reproduces the main component of the s -process of the solar system, with $\tau_0 \sim 0.30 \text{ mb}^{-1}$ (Arlandini et al. 1999), even without any assumption of the astrophysical site of the s -process.

From their abundance data in Ba stars, Allen & Barbay (2006b) extracted abundances owing the main component of the s -process, and were able to estimate the neutron exposures for the stars of their sample, fitting σN_s curves to the observed data. For a detailed description of that procedure, we refer the reader to the respective paper. Here, we have applied a similar procedure to evaluate τ_0 in our targets. In order to test our algorithm, we downloaded from the KADoNiS⁵ database a list of neutron-capture cross-sections (at 30 keV) and computed, via χ^2 minimization, the best σN_s curve that reproduces the main component of the s -process for the

⁵ Karlsruhe Astrophysical Database of Nucleosynthesis in Stars; available at <https://www.kadonis.org/>.

solar distribution reported by Arlandini et al. (1999). With our implementation, we found $\tau_0 = 0.36 \text{ mb}^{-1}$, close to value of Arlandini et al.; in their methodology, Allen & Barbuy found $\tau_0 \sim 0.35 \text{ mb}^{-1}$. Extending that approach for HD 15096, HD 37792, HD 141804, and HD 207585, we found $\tau_0 = 0.55, 0.58, 0.75, \text{ and } 0.61 \text{ mb}^{-1}$, respectively. Figure 8 shows the best fits of the σN_s curves to the observed data. In a recent review, Lugaro et al. (2023) comment that the ^{13}C neutron source (see next section) provides neutron exposure values up to 1.0 mb^{-1} , which validates the results derived from our simple approach. Allen & Barbuy reported τ_0 values ranging from 0.187 to 1.05 mb^{-1} for the Ba stars of their sample.

6. COMPARISON WITH S-PROCESS NUCLEOSYNTHESIS MODELS

Various groups have computed theoretical s -process yields from their AGB stellar models. In particular, the models provided by the INAF group (Cristallo et al. 2009, 2011, 2015) – through the on-line FRUITY⁶ database – and Monash group (Fishlock et al. 2014; Karakas & Lugaro 2016; Karakas et al. 2018) comprise predictions for a wide range of masses ($1.0 \leq M/M_\odot \leq 8.0$) and metallicities ($-1.2 \lesssim [\text{Fe}/\text{H}] \lesssim +0.3$), which covers the interval observed in Ba stars.

TP-AGB stars provide a conducive environment for the s -process nucleosynthesis within a tenuous He-rich region (He-intershell) located between the H- and He-burning shells, which are activated alternately in this evolutionary stage (Busso et al. 1999; Straniero et al. 2006; Käppeler et al. 2011; Karakas & Lattanzio 2014; Lugaro et al. 2023). For low-mass ($1 - 3 M_\odot$) AGB stars, the $^{13}\text{C}(\alpha, n)^{16}\text{O}$ reaction provides the main supply of neutrons to feed the s -process, during the interpulse periods (H-burning shell). This reaction is efficiently activated at $T \sim 10^8 \text{ K}$, releasing within the He-intershell a relatively low neutron density, of the order of 10^{7-8} cm^{-3} (Straniero et al. 1995, 1997). The H-burning ashes accumulate in the inner layers and trigger periodically He-flashes (thermal pulses; TP) that, in turn, expand the upper layers of the stars. As a consequence, the H-burning in a shell is temporarily extinguished and a convective zone is driven in the He-intershell. Temperatures in this region can reach values high enough to activate an alternative neutron source, the $^{22}\text{Ne}(\alpha, n)^{25}\text{Mg}$ reaction. However, for low-mass AGB stars, this reaction is only marginally activated. After a limited number of TP episodes, the base of the extensive convective

envelope can deepen its base, carrying to the stellar surface (Third Dredge-Up; TDU) the by-products of the internal nucleosynthesis, rich in carbon and s -elements. The $^{22}\text{Ne}(\alpha, n)^{25}\text{Mg}$ reaction becomes the main neutron provider for AGB stars of intermediate masses ($4 - 8 M_\odot$), during the TP events, at temperatures higher than $3 \times 10^8 \text{ K}$, releasing a neutron burst of $10^{10-12} \text{ cm}^{-3}$.

The FRUITY and Monash models are based on different stellar evolution codes, which assume different physical and nuclear inputs. Additionally, these models adopt different approaches to perform their detailed nucleosynthesis computations, mainly regarding to the formation of the ^{13}C pocket, since the ^{13}C left in the He-intershell is not able to provide the required neutron densities to reproduce the observations (Busso et al. 1995, 2001; Abia et al. 2001). To address this challenge, modelers assume the occurrence of a proton ingestion in the He-intershell at the time of TDU, which leads the formation of a ^{13}C pocket in the next interpulse period and provides the neutron reservoir to the s -process (Straniero et al. 1995, 1997). However, this standard approach introduces the major uncertainty source in the predictions (see, e.g., Karakas & Lattanzio 2014). The FRUITY models self-consistently produce the ^{13}C pocket from a time-dependent convective overshoot implementation (Cristallo et al. 2009). In the Monash models, a parametric approach leads to the ^{13}C pocket formation, by artificially inserting a mass of protons (controlled by the M_{mix} parameter) in the top layers of the He-intershell during the TDU (Lugaro et al. 2012). A detailed comparison between the FRUITY and Monash models is presented by Karakas & Lugaro (2016).

In this section, we perform a target-to-target comparison between the observed abundance patterns in our stars and those predicted by the (non rotating) FRUITY and Monash models. For this, we have collected the $[\text{X}/\text{Fe}]$ ratios predicted by these models, computed after the last TP, at the AGB surface. However, the s -processed material transferred was further diluted in the atmosphere of the observed Ba star. To take these effects into account, we must introduce a dilution factor (dil) in the predictions. This parameter is defined as the ratio $\log(M_{\text{Ba}}^{\text{env}}/M_{\text{AGB}}^{\text{transf}})$, where $M_{\text{Ba}}^{\text{env}}$ is the mass of the envelope of the Ba star after mass transfer and $M_{\text{AGB}}^{\text{transf}}$ is the mass transferred from the former AGB star. In this way, the diluted $[\text{X}/\text{Fe}]_{\text{Ba}}$ ratio expected to be observed in Ba stars is given by the parametric equation:

$$[\text{X}/\text{Fe}]_{\text{Ba}} = \log \left[f \times 10^{[\text{X}/\text{Fe}]_{\text{ini}}} + 10^{[\text{X}/\text{Fe}]_{\text{AGB}} - dil} \right], \quad (5)$$

where $f = 1 - 10^{dil}$, $[\text{X}/\text{Fe}]_{\text{ini}}$ is the initial (solar) composition adopted in the models and $[\text{X}/\text{Fe}]_{\text{AGB}}$ is the final

⁶ FULL-Network Repository of Updated Isotopic Tables & Yields, at <http://fruity.oa-teramo.inaf.it/>.

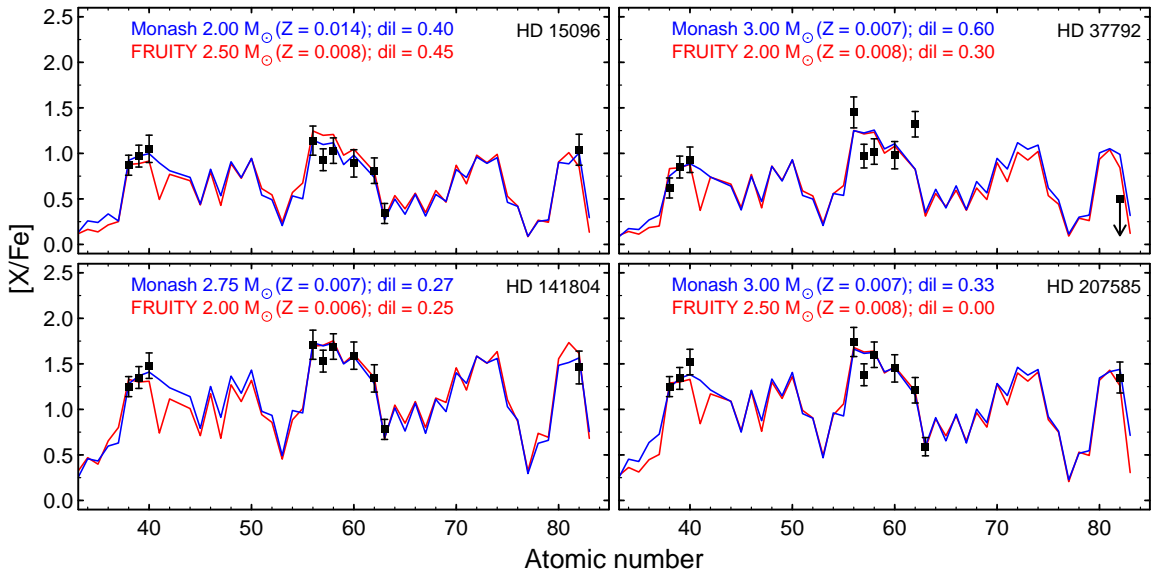


Figure 9. Comparison between the observed abundance profiles (black squares with error bars) and the predicted profiles (curves) from the Monash (blue) and FRUITY (red) nucleosynthesis models that best fit the observational data set, after dilution is applied. The derived dilution factors are also shown.

abundance predicted by the models. The dilution factor has the effect of lowering the predicted abundances but without changing the shape of the distribution. Previous studies adopted that methodology in order to derive dilution factors and infer in the mass of the AGB progenitor star (see, e.g., [Husti et al. 2009](#); [Shejeelammal et al. 2020](#); [Cseh et al. 2022](#)). We have applied different dilution factors to each model of our grid and compared the diluted predictions to the observed abundance patterns, evaluating the quality of the fits from the χ^2 values. From a χ^2 minimization, we find the models that best fit the observed data, and consequently the dilution factors.

In Figure 9, we show the neutron-capture patterns observed in HD 15096, HD 37792, HD 141804, and HD 207585, and the Monash and FRUITY models that best fit the observations. We can see that s -process nucleosynthesis models for low-mass ($\leq 3.0 M_{\odot}$) AGB stars are able to reproduce successfully our observations. In their analysis, using the FRUITY models, [Shejeelammal et al. \(2020\)](#) fitted the abundance pattern of HD 207585 with a $2.5 M_{\odot}$ ($Z = 0.008$) model. Our results are consistent with many other studies that have evidenced the low-mass nature of the former polluter TP-AGB stars that contaminated the envelope of Ba stars (e.g., [Allen & Barbuy 2006a](#); [Karinkuzhi et al. 2018b](#); [Cseh et al. 2018, 2022](#); [Shejeelammal et al. 2020](#); [den Hartogh et al. 2023](#)). In connection, this favors the ^{13}C as main neutron-source powering the s -process in low-mass AGB stars. Furthermore, if TP-AGB stars of higher masses were responsible for the patterns observed

in the program stars, it would be expected to find magnesium excesses in their atmospheres, in consequence of the operation of the ^{22}Ne neutron source. This is not observed in our stars, which exhibit normal $[\text{Mg}/\text{Fe}]$ ratios (see Tables 3 and 4). Concerning the dilution factors, low values were found ($dil \leq 0.45$), which is reasonable, since Ba dwarfs do not present extended atmospheres. [Husti et al. \(2009\)](#) reported $dil \lesssim 1.0$ for the Ba dwarfs of [Allen & Barbuy \(2006a\)](#). From the mass estimation of the polluted TP-AGB stars, we have applied the empirical initial-final mass relation of [El-Badry et al. \(2018\)](#) to constraint the masses of WD companions of our stars. We found $\langle M_{\text{WD}} \rangle \sim 0.66 M_{\odot}$, in agreement with values derived by [Escorza & De Rosa \(2023\)](#), who combined astrometric data in their analysis.

7. KINEMATICS

The kinematics properties of the Ba dwarfs analyzed in this work were obtained following the methodology outlined in [de Castro et al. \(2016\)](#). Distances and proper motions were obtained based on kinematic Gaia EDR3 data ([Gaia Collaboration 2021](#)) while radial velocities were obtained based on Doppler shift of the spectral absorption lines (Section 3.1). Then we determined the spatial velocities relative to the local standard of rest, U_{LSR} , V_{LSR} , W_{LSR} , where U_{LSR} is positive toward the Galactic center, V_{LSR} is positive in direction of Galactic rotation ($l = 90^\circ$, $b = 0^\circ$), and W_{LSR} is positive toward the north Galactic pole ($b = 90^\circ$). We assumed the solar motion of $(11.1, 12.2, 7.3) \text{ km s}^{-1}$, as derived by [Schönrich et al. \(2010\)](#) and the algorithm of [Johnson & Soderblom \(1987\)](#). Finally, the probability of a Ba

dwarf star belonging to the thin disk, thick disc, or halo population was calculated, following the procedure described in [Ramírez et al. \(2013\)](#). Membership to a given population was established when the star had a probability $P_{\text{population}}$ greater than or equal to 70%. Table 9 shows the results obtained for the spatial velocities and the corresponding probabilities.

Figure 10 display the Toomre diagram of $(U_{\text{LSR}}^2 + W_{\text{LSR}}^2)^{1/2}$ versus V_{LSR} , where the stars are kinematically classified according to their spatial velocities and probabilities. In addition to the program stars, the position of some Ba dwarf stars analyzed by [Escorza et al. \(2019\)](#), [Pereira & Drake \(2011\)](#), and [Pereira \(2005\)](#) are also shown. Data for Ba giants are included in Figure 10. HD 15096, HD 37792, HD 141804, and HD 207585 exhibit kinematical properties consistent with thin disk stars, as indicated by their membership probabilities. Most of the previously analyzed Ba dwarfs also belong to the thin disk, with one exception for the star HD 6434, which can be considered as a thin-thick disc star with P_{thin} and P_{thick} probabilities of 33% and 66%, respectively.

8. CONCLUSIONS

We conducted a classical LTE analysis based on high-resolution spectroscopic data for a sample of four chemically peculiar stars. HD 15096, HD 37792, and HD 141804 were considered as potential Ba dwarf candidates, whereas HD 207585 is a known Ba dwarf star. We have determined their atmospheric parameters, from clean and sufficiently unblended Fe I and Fe II absorption lines, and compared them with values previously reported in the literature. We found effective temperatures between 5300 – 6500 K, surface gravities within the interval $3.90 \leq \log g \leq 4.50$, and $-0.55 \leq [\text{Fe}/\text{H}] \leq +0.14$.

Subsequently, chemical abundances were extracted for a set of 21 elements, including the CNO group and neutron-capture elements. We found moderate carbon excesses in these stars, with $[\text{C}/\text{Fe}]$ ratios ranging from +0.29 to +0.66, and that carbon is mainly responsible for the CNO excesses observed in their atmospheres. HD 15096 and HD 37792 show $\text{C}/\text{O} < 1$, typical for Ba stars, while HD 141804 and HD 207585 show $\text{C}/\text{O} > 1$, typical for CH stars. For the elements from sodium to nickel, these systems follow the Galactic trend. On the other hand, as far as the s -process elements are concerned, the program stars show high levels of enrichment, with $[s/\text{Fe}] \gtrsim +1.00$ dex. All these stars are identified as spectroscopic binaries in the SIMBAD database, and orbital elements are provided in the literature for HD 15096, HD 141804, and HD 207585.

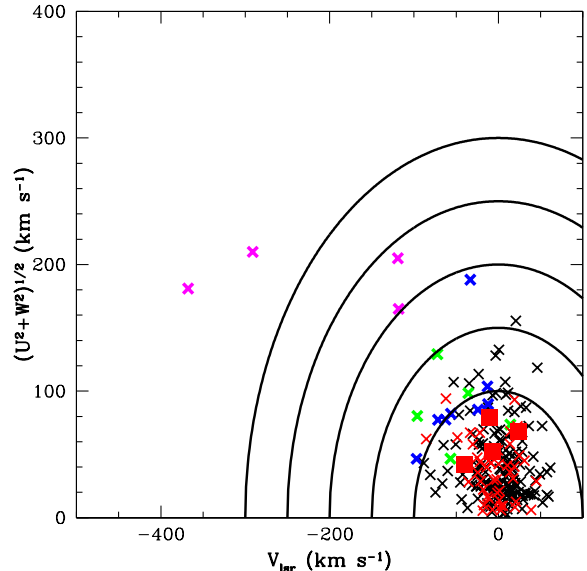


Figure 10. The Ba dwarfs analyzed in this work (red squares) in the Toomre diagram of $(U_{\text{LSR}}^2 + W_{\text{LSR}}^2)^{1/2}$ versus V_{LSR} . Ba dwarfs previously analyzed by [Escorza et al. \(2019\)](#), [Pereira & Drake \(2011\)](#), and [Pereira \(2005\)](#) are shown in red crosses. Classical Ba giant stars of the thin disk (black crosses), transition thin/thick disk (green crosses), thick disk (blue crosses), and halo (magenta crosses), taken from [de Castro et al. \(2016\)](#), are also plotted in this diagram.

Hence, their chemical peculiarities are attributable to mass transfer events. We applied the classical approach of the s -process (the σN_s curve) to estimate the neutron exposure of the s -processed material observed in their envelopes, yielding τ_0 of the order of 0.6 to 0.7 mb^{-1} .

We individually compared the observed abundance patterns in our stars with Monash and FRUITY nucleosynthesis models of the s -process. Consequently, we were able to estimate dilution factors and masses of the former polluting TP-AGB stars. Low-mass ($M \lesssim 3.0 M_{\odot}$) models successfully reproduced our observations. Notably, no Na enrichment was detected in the program stars, providing additional evidence for the operation of the ^{13}C as main neutron source of the TP-AGB stars. We applied the empirical initial-final mass relation of [El-Badry et al. \(2018\)](#) to estimate the masses of the WD companions of our stars, yielding

Table 9. Kinematic data for the Ba dwarfs analyzed in this work. The radial velocities are given in the second column. The spacial velocities with their respective uncertainties are given from the third to fifth columns. The sixth, seventh, and eighth columns give the probability of a star to be a member of the thin disk (P_{thin}), thick disk (P_{thick}) and the halo (P_{halo}). The last column gives the spatial velocity of the star.

Star	RV km s^{-1}	U_{LSR} km s^{-1}	V_{LSR} km s^{-1}	W_{LSR} km s^{-1}	P_{thin}	P_{thick}	P_{halo}
HD 15096	-5.62 ± 0.19	-30.5 ± 0.5	-7.0 ± 0.2	$+42.5 \pm 0.4$	0.95	0.05	0.00
HD 37792	$+10.13 \pm 0.44$	$+56.0 \pm 1.5$	-10.7 ± 0.6	-56.5 ± 1.7	0.76	0.23	0.00
HD 141806	-55.30 ± 0.41	-47.4 ± 0.4	$+23.4 \pm 0.4$	-10.8 ± 0.3	0.98	0.02	0.00
HD 207585	-55.89 ± 0.31	-21.6 ± 0.2	-39.7 ± 1.4	$+35.8 \pm 0.6$	0.88	0.12	0.00

$\langle M_{\text{WD}} \rangle \sim 0.66 M_{\odot}$, which is consistent for Ba and related stars. From the kinematic point of view, we estimated the probabilities of these stars belonging to thin disc, thick disc, and halo. We found that these objects are members of thin disc, with probabilities greater than 70%.

In conclusion, we have identified HD 15096 and HD 37792 as two new Ba dwarfs, and confirmed the Ba dwarf nature of HD 141804. As we pointed out, the current sample of Ba dwarfs confirmed from high-resolution spectroscopic data is much smaller than the sample of the classical giants. Finally, we stressed on the need of identifying new Ba dwarf star candidates and exploring their chemical patterns.

ACKNOWLEDGMENTS

This work has been developed under a fellowship of the PCI Program of the Ministry of Science, Technol-

ogy and Innovation - MCTI, financed by the Brazilian National Council of Research - CNPq, through the grant 300438/2024-9. NH acknowledges the fellowships (300181/2023-0 and 300434/2024-3) of the PCI Program - MCTI and CNPq. NAD acknowledges Fundação de Amparo à Pesquisa do Estado do Rio de Janeiro - FAPERJ, Rio de Janeiro, Brazil, for grant E-26/203.847/2022. AS acknowledges CNPq for a PhD fellowship 141219/2023-8. This work has made use of the VALD database, operated at Uppsala University, the Institute of Astronomy RAS in Moscow, and the University of Vienna. This research has made use of NASA's Astrophysics Data System Bibliographic Services.

Facilities:

Software: IRAF (Tody 1986); MOOG (Snedden 1973; Sneden et al. 2012); R and RStudio (R Core Team 2021)

REFERENCES

- Abia, C., Busso, M., Gallino, R., et al. 2001, ApJ, 559, 1117, doi: [10.1086/322383](https://doi.org/10.1086/322383)
- Allen, D. M., & Barbuy, B. 2006a, A&A, 454, 895, doi: [10.1051/0004-6361:20064912](https://doi.org/10.1051/0004-6361:20064912)
- . 2006b, A&A, 454, 917, doi: [10.1051/0004-6361:20064968](https://doi.org/10.1051/0004-6361:20064968)
- Allende Prieto, C., Lambert, D. L., & Asplund, M. 2001, ApJL, 556, L63, doi: [10.1086/322874](https://doi.org/10.1086/322874)
- Alonso, A., Arribas, S., & Martinez-Roger, C. 1995, A&A, 297, 197
- Amarsi, A. M., Asplund, M., Collet, R., & Leenaarts, J. 2015, MNRAS, 454, L11, doi: [10.1093/mnras/171/2/122](https://doi.org/10.1093/mnras/171/2/122)
- Antipova, L. I., Boyarchuk, A. A., Pakhomov, Y. V., & Panchuk, V. E. 2004, Astronomy Reports, 48, 597, doi: [10.1134/1.1777277](https://doi.org/10.1134/1.1777277)
- Arlandini, C., Käppeler, F., Wisshak, K., et al. 1999, ApJ, 525, 886, doi: [10.1086/307938](https://doi.org/10.1086/307938)
- Barbuy, B., Jorissen, A., Rossi, S. C. F., & Arnould, M. 1992, A&A, 262, 216
- Beers, T. C., & Christlieb, N. 2005, ARA&A, 43, 531, doi: [10.1146/annurev.astro.42.053102.134057](https://doi.org/10.1146/annurev.astro.42.053102.134057)
- Bessell, M. S., Castelli, F., & Plez, B. 1998, A&A, 333, 231
- Bidelman, W. P., & Keenan, P. C. 1951, ApJ, 114, 473, doi: [10.1086/145488](https://doi.org/10.1086/145488)
- Bisterzo, S., Travaglio, C., Gallino, R., Wiescher, M., & Käppeler, F. 2014, ApJ, 787, 10, doi: [10.1088/0004-637X/787/1/10](https://doi.org/10.1088/0004-637X/787/1/10)
- Bond, H. E. 1974, ApJ, 194, 95, doi: [10.1086/153227](https://doi.org/10.1086/153227)
- Boothroyd, A. I., Sackmann, I. J., & Wasserburg, G. J. 1995, ApJL, 442, L21, doi: [10.1086/187806](https://doi.org/10.1086/187806)
- Bressan, A., Marigo, P., Girardi, L., et al. 2012, MNRAS, 427, 127, doi: [10.1111/j.1365-2966.2012.21948.x](https://doi.org/10.1111/j.1365-2966.2012.21948.x)
- Burbidge, E. M., Burbidge, G. R., Fowler, W. A., & Hoyle, F. 1957, Reviews of Modern Physics, 29, 547, doi: [10.1103/RevModPhys.29.547](https://doi.org/10.1103/RevModPhys.29.547)
- Busso, M., Gallino, R., Lambert, D. L., Travaglio, C., & Smith, V. V. 2001, ApJ, 557, 802, doi: [10.1086/322258](https://doi.org/10.1086/322258)

- Busso, M., Gallino, R., & Wasserburg, G. J. 1999, *ARA&A*, 37, 239, doi: [10.1146/annurev.astro.37.1.239](https://doi.org/10.1146/annurev.astro.37.1.239)
- Busso, M., Lambert, D. L., Beglio, L., et al. 1995, *ApJ*, 446, 775, doi: [10.1086/175835](https://doi.org/10.1086/175835)
- Carretta, E., Bragaglia, A., & Gratton, R. G. 2007, *A&A*, 473, 129, doi: [10.1051/0004-6361:20065213](https://doi.org/10.1051/0004-6361:20065213)
- Chen, B., Vergely, J. L., Valette, B., & Carraro, G. 1998, *A&A*, 336, 137, doi: [10.48550/arXiv.astro-ph/9805018](https://doi.org/10.48550/arXiv.astro-ph/9805018)
- Chen, Y. Q., Zhao, G., Nissen, P. E., Bai, G. S., & Qiu, H. M. 2003, *ApJ*, 591, 925, doi: [10.1086/375292](https://doi.org/10.1086/375292)
- Cowan, J. J., Sneden, C., Lawler, J. E., et al. 2021, *Reviews of Modern Physics*, 93, 015002, doi: [10.1103/RevModPhys.93.015002](https://doi.org/10.1103/RevModPhys.93.015002)
- Cristallo, S., Straniero, O., Gallino, R., et al. 2009, *ApJ*, 696, 797, doi: [10.1088/0004-637X/696/1/797](https://doi.org/10.1088/0004-637X/696/1/797)
- Cristallo, S., Straniero, O., Piersanti, L., & Gobrecht, D. 2015, *ApJS*, 219, 40, doi: [10.1088/0067-0049/219/2/40](https://doi.org/10.1088/0067-0049/219/2/40)
- Cristallo, S., Piersanti, L., Straniero, O., et al. 2011, *ApJS*, 197, 17, doi: [10.1088/0067-0049/197/2/17](https://doi.org/10.1088/0067-0049/197/2/17)
- Cseh, B., Lugaro, M., D'Orazi, V., et al. 2018, *A&A*, 620, A146, doi: [10.1051/0004-6361/201834079](https://doi.org/10.1051/0004-6361/201834079)
- Cseh, B., Világos, B., Roriz, M. P., et al. 2022, *A&A*, 660, A128, doi: [10.1051/0004-6361/202142468](https://doi.org/10.1051/0004-6361/202142468)
- da Silva, L., Girardi, L., Pasquini, L., et al. 2006, *A&A*, 458, 609, doi: [10.1051/0004-6361:20065105](https://doi.org/10.1051/0004-6361:20065105)
- de Castro, D. B., Pereira, C. B., Roig, F., et al. 2016, *MNRAS*, 459, 4299, doi: [10.1093/mnras/stw815](https://doi.org/10.1093/mnras/stw815)
- de Strobel, G. C., & Spite, M. 1988, *The Impact of Very High S/N Spectroscopy on Stellar Physics: Proceedings of the 132nd Symposium of the International Astronomical Union Held in Paris, France, June 29-July 3, 1987 No. 132* (Springer Science & Business Media)
- Den Hartog, E. A., Lawler, J. E., Sneden, C., & Cowan, J. J. 2003, *ApJS*, 148, 543, doi: [10.1086/376940](https://doi.org/10.1086/376940)
- den Hartogh, J. W., Yagüe López, A., Cseh, B., et al. 2023, *A&A*, 672, A143, doi: [10.1051/0004-6361/202244189](https://doi.org/10.1051/0004-6361/202244189)
- Depagne, E., Hill, V., Spite, M., et al. 2002, *A&A*, 390, 187, doi: [10.1051/0004-6361:20020687](https://doi.org/10.1051/0004-6361:20020687)
- Drake, J. J., & Smith, G. 1991, *MNRAS*, 250, 89, doi: [10.1093/mnras/250.1.89](https://doi.org/10.1093/mnras/250.1.89)
- Drake, N. A., & Pereira, C. B. 2007, in *Convection in Astrophysics*, ed. F. Kupka, I. Roxburgh, & K. L. Chan, Vol. 239, 304–306, doi: [10.1017/S1743921307000610](https://doi.org/10.1017/S1743921307000610)
- Drake, N. A., & Pereira, C. B. 2008, *AJ*, 135, 1070, doi: [10.1088/0004-6256/135/3/1070](https://doi.org/10.1088/0004-6256/135/3/1070)
- Edvardsson, B., Andersen, J., Gustafsson, B., et al. 1993, *A&A*, 500, 391
- El-Badry, K., Rix, H.-W., & Weisz, D. R. 2018, *ApJL*, 860, L17, doi: [10.3847/2041-8213/aaca9c](https://doi.org/10.3847/2041-8213/aaca9c)
- Escorza, A., & De Rosa, R. J. 2023, *A&A*, 671, A97, doi: [10.1051/0004-6361/202244782](https://doi.org/10.1051/0004-6361/202244782)
- Escorza, A., Siess, L., Van Winckel, H., & Jorissen, A. 2020, *A&A*, 639, A24, doi: [10.1051/0004-6361/202037487](https://doi.org/10.1051/0004-6361/202037487)
- Escorza, A., Boffin, H. M. J., Jorissen, A., et al. 2017, *A&A*, 608, A100, doi: [10.1051/0004-6361/201731832](https://doi.org/10.1051/0004-6361/201731832)
- Escorza, A., Karinkuzhi, D., Jorissen, A., et al. 2019, *A&A*, 626, A128, doi: [10.1051/0004-6361/201935390](https://doi.org/10.1051/0004-6361/201935390)
- Fishlock, C. K., Karakas, A. I., Lugaro, M., & Yong, D. 2014, *ApJ*, 797, 44, doi: [10.1088/0004-637X/797/1/44](https://doi.org/10.1088/0004-637X/797/1/44)
- Frantsman, Y. L. 1992, *Soviet Ast.*, 36, 155
- Fulbright, J. P. 2000, *AJ*, 120, 1841, doi: [10.1086/301548](https://doi.org/10.1086/301548)
- Gaia Collaboration. 2020, *VizieR Online Data Catalog*, I/350
- . 2021, *A&A*, 649, A1, doi: [10.1051/0004-6361/202039657](https://doi.org/10.1051/0004-6361/202039657)
- Gallino, R., Arlandini, C., Busso, M., et al. 1998, *ApJ*, 497, 388, doi: [10.1086/305437](https://doi.org/10.1086/305437)
- Goswami, A., Aoki, W., Beers, T. C., et al. 2006, *MNRAS*, 372, 343, doi: [10.1111/j.1365-2966.2006.10877.x](https://doi.org/10.1111/j.1365-2966.2006.10877.x)
- Goswami, A., Aoki, W., & Karinkuzhi, D. 2016, *MNRAS*, 455, 402, doi: [10.1093/mnras/stv201110.48550/arXiv.1510.07814](https://doi.org/10.1093/mnras/stv201110.48550/arXiv.1510.07814)
- Gratton, R. G., Carretta, E., Claudi, R., Lucatello, S., & Barbieri, M. 2003, *A&A*, 404, 187, doi: [10.1051/0004-6361:20030439](https://doi.org/10.1051/0004-6361:20030439)
- Grevesse, N., & Sauval, A. J. 1998, *SSRv*, 85, 161, doi: [10.1023/A:1005161325181](https://doi.org/10.1023/A:1005161325181)
- Guo, F., Cheng, Z., Kong, X., et al. 2023, *AJ*, 165, 40, doi: [10.3847/1538-3881/aca323](https://doi.org/10.3847/1538-3881/aca323)
- Han, Z., Eggleton, P. P., Podsiadlowski, P., & Tout, C. A. 1995, *MNRAS*, 277, 1443, doi: [10.1093/mnras/277.4.1443](https://doi.org/10.1093/mnras/277.4.1443)
- Holanda, N., Drake, N. A., & Pereira, C. B. 2020, *MNRAS*, 498, 77, doi: [10.1093/mnras/staa2271](https://doi.org/10.1093/mnras/staa2271)
- . 2023, *MNRAS*, 518, 4038, doi: [10.1093/mnras/stac3343](https://doi.org/10.1093/mnras/stac3343)
- Husti, L., Gallino, R., Bisterzo, S., Straniero, O., & Cristallo, S. 2009, *PASA*, 26, 176, doi: [10.1071/AS08065](https://doi.org/10.1071/AS08065)
- Johnson, D. R. H., & Soderblom, D. R. 1987, *AJ*, 93, 864, doi: [10.1086/114370](https://doi.org/10.1086/114370)
- Johnson, J. A., Ivans, I. I., & Stetson, P. B. 2006, *ApJ*, 640, 801, doi: [10.1086/498882](https://doi.org/10.1086/498882)
- Jorissen, A., Boffin, H. M. J., Karinkuzhi, D., et al. 2019, *A&A*, 626, A127, doi: [10.1051/0004-6361/201834630](https://doi.org/10.1051/0004-6361/201834630)
- Jorissen, A., Van Eck, S., Mayor, M., & Udry, S. 1998, *A&A*, 332, 877. <https://arxiv.org/abs/astro-ph/9801272>
- Jorissen, A., Van Eck, S., Van Winckel, H., et al. 2016, *A&A*, 586, A158, doi: [10.1051/0004-6361/201526992](https://doi.org/10.1051/0004-6361/201526992)
- Kaeppler, F., Gallino, R., Busso, M., Picchio, G., & Raiteri, C. M. 1990, *ApJ*, 354, 630, doi: [10.1086/168720](https://doi.org/10.1086/168720)

- Käppeler, F., Gallino, R., Bisterzo, S., & Aoki, W. 2011, *Reviews of Modern Physics*, 83, 157, doi: [10.1103/RevModPhys.83.157](https://doi.org/10.1103/RevModPhys.83.157)
- Karakas, A. I., & Lattanzio, J. C. 2014, *PASA*, 31, e030, doi: [10.1017/pasa.2014.21](https://doi.org/10.1017/pasa.2014.21)
- Karakas, A. I., & Lugaro, M. 2016, *ApJ*, 825, 26, doi: [10.3847/0004-637X/825/1/26](https://doi.org/10.3847/0004-637X/825/1/26)
- Karakas, A. I., Lugaro, M., Carlos, M., et al. 2018, *MNRAS*, 477, 421, doi: [10.1093/mnras/sty625](https://doi.org/10.1093/mnras/sty625)
- Karinkuzhi, D., & Goswami, A. 2014, *MNRAS*, 440, 1095, doi: [10.1093/mnras/stu14810.48550/arXiv.1410.0111](https://doi.org/10.1093/mnras/stu14810.48550/arXiv.1410.0111)
- . 2015, *MNRAS*, 446, 2348, doi: [10.1093/mnras/stu2079](https://doi.org/10.1093/mnras/stu2079)
- Karinkuzhi, D., Goswami, A., Sridhar, N., Masseron, T., & Purandardas, M. 2018a, *MNRAS*, 476, 3086, doi: [10.1093/mnras/sty32010.48550/arXiv.1802.01343](https://doi.org/10.1093/mnras/sty32010.48550/arXiv.1802.01343)
- Karinkuzhi, D., Van Eck, S., Jorissen, A., et al. 2018b, *A&A*, 618, A32, doi: [10.1051/0004-6361/201833084](https://doi.org/10.1051/0004-6361/201833084)
- . 2021, *A&A*, 654, A140, doi: [10.1051/0004-6361/202141629](https://doi.org/10.1051/0004-6361/202141629)
- Kaufer, A., Stahl, O., Tubbesing, S., et al. 1999, *The Messenger*, 95, 8
- Keenan, P. C. 1942, *ApJ*, 96, 101, doi: [10.1086/144435](https://doi.org/10.1086/144435)
- Kong, X. M., Bharat Kumar, Y., Zhao, G., et al. 2018, *MNRAS*, 474, 2129, doi: [10.1093/mnras/stx280910.48550/arXiv.1710.10750](https://doi.org/10.1093/mnras/stx280910.48550/arXiv.1710.10750)
- Kurucz, R. 1993, *ATLAS9 Stellar Atmosphere Programs and 2 km/s grid*. Kurucz CD-ROM No. 13. Cambridge, 13
- Lambert, D. L., Heath, J. E., Lemke, M., & Drake, J. 1996, *ApJS*, 103, 183, doi: [10.1086/192274](https://doi.org/10.1086/192274)
- Lambert, D. L., Roby, S. W., & Bell, R. A. 1982, *ApJ*, 254, 663, doi: [10.1086/159777](https://doi.org/10.1086/159777)
- Latham, D. W., Stefanik, R. P., Torres, G., et al. 2002, *AJ*, 124, 1144, doi: [10.1086/341384](https://doi.org/10.1086/341384)
- Lawler, J. E., Bonvallet, G., & Sneden, C. 2001a, *ApJ*, 556, 452, doi: [10.1086/321549](https://doi.org/10.1086/321549)
- Lawler, J. E., Den Hartog, E. A., Sneden, C., & Cowan, J. J. 2006, *ApJS*, 162, 227, doi: [10.1086/498213](https://doi.org/10.1086/498213)
- Lawler, J. E., Guzman, A., Wood, M. P., Sneden, C., & Cowan, J. J. 2013, *ApJS*, 205, 11, doi: [10.1088/0067-0049/205/2/11](https://doi.org/10.1088/0067-0049/205/2/11)
- Lawler, J. E., Sneden, C., Cowan, J. J., Ivans, I. I., & Den Hartog, E. A. 2009, *ApJS*, 182, 51, doi: [10.1088/0067-0049/182/1/51](https://doi.org/10.1088/0067-0049/182/1/51)
- Lawler, J. E., Wickliffe, M. E., den Hartog, E. A., & Sneden, C. 2001b, *ApJ*, 563, 1075, doi: [10.1086/323407](https://doi.org/10.1086/323407)
- Liu, S., Wang, L., Shi, J.-R., et al. 2021, *Research in Astronomy and Astrophysics*, 21, 278, doi: [10.1088/1674-4527/21/11/278](https://doi.org/10.1088/1674-4527/21/11/278)
- Ljung, G., Nilsson, H., Asplund, M., & Johansson, S. 2006, *A&A*, 456, 1181, doi: [10.1051/0004-6361:20065212](https://doi.org/10.1051/0004-6361:20065212)
- Luck, R. E., & Bond, H. E. 1982, *ApJ*, 259, 792, doi: [10.1086/160215](https://doi.org/10.1086/160215)
- . 1991, *ApJS*, 77, 515, doi: [10.1086/191615](https://doi.org/10.1086/191615)
- Luck, R. E., & Heiter, U. 2006, *AJ*, 131, 3069, doi: [10.1086/504080](https://doi.org/10.1086/504080)
- . 2007, *AJ*, 133, 2464, doi: [10.1086/513194](https://doi.org/10.1086/513194)
- Lugaro, M., Karakas, A. I., Stancliffe, R. J., & Rijs, C. 2012, *ApJ*, 747, 2, doi: [10.1088/0004-637X/747/1/2](https://doi.org/10.1088/0004-637X/747/1/2)
- Lugaro, M., Pignatari, M., Reifarth, R., & Wiescher, M. 2023, *Annual Review of Nuclear and Particle Science*, 73, 315, doi: [10.1146/annurev-nucl-102422-080857](https://doi.org/10.1146/annurev-nucl-102422-080857)
- Masseron, T., Johnson, J. A., Plez, B., et al. 2010, *A&A*, 509, A93, doi: [10.1051/0004-6361/200911744](https://doi.org/10.1051/0004-6361/200911744)
- McClure, R. D. 1984, *ApJL*, 280, L31, doi: [10.1086/184263](https://doi.org/10.1086/184263)
- McClure, R. D., Fletcher, J. M., & Nemeč, J. M. 1980, *ApJL*, 238, L35, doi: [10.1086/183252](https://doi.org/10.1086/183252)
- McClure, R. D., & Woodsworth, A. W. 1990, *ApJ*, 352, 709, doi: [10.1086/168573](https://doi.org/10.1086/168573)
- McWilliam, A. 1998, *AJ*, 115, 1640, doi: [10.1086/300289](https://doi.org/10.1086/300289)
- McWilliam, A., & Rich, R. M. 1994, *ApJS*, 91, 749, doi: [10.1086/191954](https://doi.org/10.1086/191954)
- Mowlavi, N. 1999, *A&A*, 350, 73, doi: [10.48550/arXiv.astro-ph/9910542](https://doi.org/10.48550/arXiv.astro-ph/9910542)
- Norfolk, B. J., Casey, A. R., Karakas, A. I., et al. 2019, *MNRAS*, 490, 2219, doi: [10.1093/mnras/stz2630](https://doi.org/10.1093/mnras/stz2630)
- Norris, J. E., Ryan, S. G., & Beers, T. C. 1996, *ApJS*, 107, 391, doi: [10.1086/192368](https://doi.org/10.1086/192368)
- North, P., Berthet, S., & Lanz, T. 1994, *A&A*, 281, 775
- North, P. L., Jorissen, A., Escorza, A., Miszalski, B., & Mikolajewska, J. 2020, *The Observatory*, 140, 11. <https://arxiv.org/abs/2001.11319>
- Pereira, C. B. 2005, *AJ*, 129, 2469, doi: [10.1086/428755](https://doi.org/10.1086/428755)
- Pereira, C. B., & Drake, N. A. 2009, *A&A*, 496, 791, doi: [10.1051/0004-6361/200810851](https://doi.org/10.1051/0004-6361/200810851)
- . 2011, *AJ*, 141, 79, doi: [10.1088/0004-6256/141/3/79](https://doi.org/10.1088/0004-6256/141/3/79)
- Pereira, C. B., Drake, N. A., & Roig, F. 2019, *MNRAS*, 488, 482, doi: [10.1093/mnras/stz1411](https://doi.org/10.1093/mnras/stz1411)
- Pereira, C. B., Jilinski, E., Drake, N. A., et al. 2012, *A&A*, 543, A58, doi: [10.1051/0004-6361/201219122](https://doi.org/10.1051/0004-6361/201219122)
- Pereira, C. B., & Junqueira, S. 2003, *A&A*, 402, 1061, doi: [10.1051/0004-6361:20030209](https://doi.org/10.1051/0004-6361:20030209)
- Pereira, C. B., Sales Silva, J. V., Chavero, C., Roig, F., & Jilinski, E. 2011, *A&A*, 533, A51, doi: [10.1051/0004-6361/201117070](https://doi.org/10.1051/0004-6361/201117070)
- Porto de Mello, G. F., & da Silva, L. 1997, *ApJL*, 476, L89, doi: [10.1086/310504](https://doi.org/10.1086/310504)

- Pourbaix, D., Tokovinin, A. A., Batten, A. H., et al. 2004, *A&A*, 424, 727, doi: [10.1051/0004-6361:2004121310.48550/arXiv.astro-ph/0406573](https://doi.org/10.1051/0004-6361:2004121310.48550/arXiv.astro-ph/0406573)
- Preston, G. W., & Sneden, C. 2001, *AJ*, 122, 1545, doi: [10.1086/322082](https://doi.org/10.1086/322082)
- Purandardas, M., Goswami, A., Goswami, P. P., Shejeelammal, J., & Masseron, T. 2019, *MNRAS*, 486, 3266, doi: [10.1093/mnras/stz75910.48550/arXiv.1904.03904](https://doi.org/10.1093/mnras/stz75910.48550/arXiv.1904.03904)
- R Core Team. 2021, *R: A Language and Environment for Statistical Computing*, R Foundation for Statistical Computing, Vienna, Austria. <https://www.R-project.org/>
- Ramírez, I., Allende Prieto, C., & Lambert, D. L. 2013, *ApJ*, 764, 78, doi: [10.1088/0004-637X/764/1/78](https://doi.org/10.1088/0004-637X/764/1/78)
- Reddy, B. E., Bakker, E. J., & Hrivnak, B. J. 1999, *ApJ*, 524, 831, doi: [10.1086/307858](https://doi.org/10.1086/307858)
- Reddy, B. E., Lambert, D. L., & Allende Prieto, C. 2006, *MNRAS*, 367, 1329, doi: [10.1111/j.1365-2966.2006.10148.x10.48550/arXiv.astro-ph/0512505](https://doi.org/10.1111/j.1365-2966.2006.10148.x10.48550/arXiv.astro-ph/0512505)
- Reddy, B. E., Tomkin, J., Lambert, D. L., & Allende Prieto, C. 2003, *MNRAS*, 340, 304, doi: [10.1046/j.1365-8711.2003.06305.x](https://doi.org/10.1046/j.1365-8711.2003.06305.x)
- Reyniers, M., Van Winckel, H., Gallino, R., & Straniero, O. 2004, *A&A*, 417, 269, doi: [10.1051/0004-6361:20034397](https://doi.org/10.1051/0004-6361:20034397)
- Roriz, M., Pereira, C. B., Drake, N. A., Roig, F., & Silva, J. V. S. 2017, *MNRAS*, 472, 350, doi: [10.1093/mnras/stx1930](https://doi.org/10.1093/mnras/stx1930)
- Roriz, M. P., Lugaro, M., Pereira, C. B., et al. 2021a, *MNRAS*, 501, 5834, doi: [10.1093/mnras/staa3888](https://doi.org/10.1093/mnras/staa3888)
- . 2021b, *MNRAS*, 507, 1956, doi: [10.1093/mnras/stab2014](https://doi.org/10.1093/mnras/stab2014)
- Roriz, M. P., Pereira, C. B., Junqueira, S., et al. 2023, *MNRAS*, 518, 5414, doi: [10.1093/mnras/stac3378](https://doi.org/10.1093/mnras/stac3378)
- Ryabchikova, T., Piskunov, N., Kurucz, R. L., et al. 2015, A major upgrade of the VALD database, [Online]. Available: <http://vald.astro.uu.se/>, doi: [10.1088/0031-8949/90/5/054005](https://doi.org/10.1088/0031-8949/90/5/054005)
- Schönrich, R., Binney, J., & Dehnen, W. 2010, *MNRAS*, 403, 1829, doi: [10.1111/j.1365-2966.2010.16253.x](https://doi.org/10.1111/j.1365-2966.2010.16253.x)
- Shejeelammal, J., Goswami, A., Goswami, P. P., Rathour, R. S., & Masseron, T. 2020, *MNRAS*, 492, 3708, doi: [10.1093/mnras/stz3518](https://doi.org/10.1093/mnras/stz3518)
- Smith, G., Edvardsson, B., & Frisk, U. 1986, *A&A*, 165, 126
- Smith, V. V., Coleman, H., & Lambert, D. L. 1993, *ApJ*, 417, 287, doi: [10.1086/173311](https://doi.org/10.1086/173311)
- Smith, V. V., & Lambert, D. L. 1986, *ApJ*, 303, 226, doi: [10.1086/164068](https://doi.org/10.1086/164068)
- Sneden, C., Bean, J., Ivans, I., Lucatello, S., & Sobeck, J. 2012, MOOG: LTE line analysis and spectrum synthesis, Astrophysics Source Code Library, record ascl:1202.009. <http://ascl.net/1202.009>
- Sneden, C., & Bond, H. E. 1976, *ApJ*, 204, 810, doi: [10.1086/154229](https://doi.org/10.1086/154229)
- Sneden, C., McWilliam, A., Preston, G. W., et al. 1996, *ApJ*, 467, 819, doi: [10.1086/177656](https://doi.org/10.1086/177656)
- Sneden, C. A. 1973, PhD thesis, THE UNIVERSITY OF TEXAS AT AUSTIN.
- Sobeck, J. S., Lawler, J. E., & Sneden, C. 2007, *ApJ*, 667, 1267, doi: [10.1086/519987](https://doi.org/10.1086/519987)
- Soubiran, C., & Girard, P. 2005, *A&A*, 438, 139, doi: [10.1051/0004-6361:20042390](https://doi.org/10.1051/0004-6361:20042390)
- Straniero, O., Chieffi, A., Limongi, M., et al. 1997, *ApJ*, 478, 332, doi: [10.1086/303794](https://doi.org/10.1086/303794)
- Straniero, O., Gallino, R., Busso, M., et al. 1995, *ApJL*, 440, L85, doi: [10.1086/187767](https://doi.org/10.1086/187767)
- Straniero, O., Gallino, R., & Cristallo, S. 2006, *NuPhA*, 777, 311, doi: [10.1016/j.nuclphysa.2005.01.011](https://doi.org/10.1016/j.nuclphysa.2005.01.011)
- Takeda, Y., & Honda, S. 2005, *PASJ*, 57, 65, doi: [10.1093/pasj/57.1.65](https://doi.org/10.1093/pasj/57.1.65)
- Takeda, Y., & Sadakane, K. 1997, *PASJ*, 49, 571, doi: [10.1093/pasj/49.5.571](https://doi.org/10.1093/pasj/49.5.571)
- Takeda, Y., Parthasarathy, M., Aoki, W., et al. 2002, *PASJ*, 54, 765, doi: [10.1093/pasj/54.5.765](https://doi.org/10.1093/pasj/54.5.765)
- Tody, D. 1986, in *Society of Photo-Optical Instrumentation Engineers (SPIE) Conference Series*, Vol. 627, *Instrumentation in astronomy VI*, ed. D. L. Crawford, 733, doi: [10.1117/12.968154](https://doi.org/10.1117/12.968154)
- Tomkin, J., Lambert, D. L., Edvardsson, B., Gustafsson, B., & Nissen, P. E. 1989, *A&A*, 219, L15
- Van Eck, S., Goriely, S., Jorissen, A., & Plez, B. 2003, *A&A*, 404, 291, doi: [10.1051/0004-6361:20030447](https://doi.org/10.1051/0004-6361:20030447)
- Van Winckel, H., & Reyniers, M. 2000, *A&A*, 354, 135. <https://arxiv.org/abs/astro-ph/9910112>
- Wiese, W. L., Smith, M. W., & Miles, B. M. 1969, *Atomic transition probabilities*. Vol. 2: Sodium through Calcium. A critical data compilation
- Wood, M. P., Lawler, J. E., Sneden, C., & Cowan, J. J. 2014, *ApJS*, 211, 20, doi: [10.1088/0067-0049/211/2/20](https://doi.org/10.1088/0067-0049/211/2/20)
- Woolley, S. E., & Weaver, T. A. 1995, *ApJS*, 101, 181, doi: [10.1086/192237](https://doi.org/10.1086/192237)
- Zacharias, N., Monet, D. G., Levine, S. E., et al. 2004, in *American Astronomical Society Meeting Abstracts*, Vol. 205, American Astronomical Society Meeting Abstracts, 48.15

APPENDIX

Table A1. Equivalent width measurements of Fe I and Fe II lines.

Element	Wavelength	χ (eV)	log gf	Equivalent widths (mÅ)			
				HD 15096	HD 37792	HD 141804	HD 207585
Fe I	5 133.69	4.18	+0.20	—	—	108	—
	5 150.84	0.99	-3.00	135	58	75	—
	5 151.91	1.01	-3.32	—	41	—	—
	5 159.06	4.28	-0.65	77	28	39	53
	5 162.27	4.18	+0.07	—	80	—	—
	5 194.94	1.56	-2.09	—	80	91	109
	5 198.71	2.22	-2.14	111	49	63	76
	5 232.94	2.94	-0.08	—	117	—	—
	5 242.49	3.63	-0.97	93	48	54	71
	5 250.21	0.12	-4.92	80	—	—	50
	5 281.79	3.04	-0.83	—	83	91	108
	5 288.52	3.69	-1.51	65	18	27	40
	5 302.31	3.28	-0.74	—	72	—	—
	5 307.36	1.61	-2.97	96	38	54	70
	5 321.11	4.43	-1.19	49	—	—	—
	5 322.04	2.28	-2.84	68	—	26	40
	5 339.93	3.27	-0.68	—	76	90	102
	5 341.02	1.61	-1.95	—	87	103	128
	5 353.37	4.10	-0.68	95	—	—	—
	5 364.87	4.45	+0.23	—	73	80	93
	5 367.47	4.42	+0.43	—	76	—	103
	5 373.71	4.47	-0.71	66	25	32	46
	5 389.48	4.42	-0.25	—	41	54	64
	5 393.17	3.24	-0.72	—	72	—	—
	5 400.50	4.37	-0.10	125	59	79	—
	5 405.77	0.99	-1.85	—	111	—	—
	5 410.91	4.47	+0.40	—	73	—	109
	5 417.03	4.42	-1.53	35	—	—	—
	5 434.52	1.01	-2.12	—	103	—	—
	5 441.34	4.31	-1.58	38	—	—	—
	5 445.04	4.39	+0.04	—	64	—	86
	5 446.92	0.99	-1.91	—	112	—	—
	5 487.75	4.32	-0.65	86	41	—	—
	5 506.78	0.99	-2.80	—	70	—	105
	5 522.45	4.21	-1.40	47	—	—	32
	5 532.75	3.57	-2.00	50	14	—	—
	5 554.90	4.55	-0.38	92	43	52	—
	5 560.21	4.43	-1.04	52	16	22	32
	5 563.60	4.19	-.840	81	31	49	—
	5 567.39	2.61	-2.56	73	—	29	—

Continued on next page

Table A1 – Continued

Element	Wavelength	χ (eV)	$\log gf$	Equivalent widths (mÅ)			
				HD 15096	HD 37792	HD 141804	HD 207585
	5 569.62	3.42	-0.49	—	74	94	—
	5 572.84	3.40	-0.28	—	89	—	—
	5 576.09	3.43	-0.85	—	58	74	—
	5 584.77	3.57	-2.17	47	—	—	—
	5 624.02	4.39	-1.33	39	—	—	—
	5 633.95	4.99	-0.12	78	29	—	—
	5 635.82	4.26	-1.74	32	—	—	—
	5 638.26	4.22	-0.72	79	—	45	60
	5 686.53	4.55	-0.45	79	—	—	56
	5 691.50	4.30	-1.37	43	—	22	30
	5 705.47	4.30	-1.36	42	—	—	22
	5 717.83	4.28	-0.97	65	—	30	44
	5 731.76	4.26	-1.15	58	16	28	43
	5 762.99	4.21	-0.41	109	61	—	78
	5 806.73	4.61	-0.90	51	15	22	33
	5 814.81	4.28	-1.82	22	—	—	14
	5 852.22	4.55	-1.18	42	—	16	23
	5 883.82	3.96	-1.21	69	19	32	47
	5 916.25	2.45	-2.99	60	10	—	37
	5 934.65	3.93	-1.02	83	25	41	64
	6 016.66	3.55	-1.67	73	—	—	—
	6 024.06	4.55	-0.06	—	57	71	80
	6 027.05	4.08	-1.09	67	22	37	49
	6 056.01	4.73	-0.40	73	29	41	48
	6 065.48	2.61	-1.53	129	63	77	92
	6 079.01	4.65	-0.97	44	14	—	27
	6 082.71	2.22	-3.58	39	—	—	—
	6 093.64	4.61	-1.35	31	—	—	17
	6 096.66	3.98	-1.78	38	—	—	18
	6 136.61	2.45	-1.40	—	80	90	103
	6 137.69	2.59	-1.40	—	71	87	103
	6 151.62	2.18	-3.29	57	—	18	30
	6 157.73	4.08	-1.11	58	23	34	—
	6 165.36	4.14	-1.47	45	16	18	27
	6 170.51	4.79	-0.38	78	31	42	55
	6 173.34	2.22	-2.88	74	20	30	49
	6 187.99	3.94	-1.57	51	—	20	28
	6 191.56	2.43	-1.42	—	75	87	107
	6 200.31	2.60	-2.44	75	20	34	52
	6 213.43	2.22	-2.48	91	30	47	62
	6 230.72	2.56	-1.28	—	83	96	109
	6 252.56	2.40	-1.72	130	66	82	97
	6 254.26	2.28	-2.44	97	—	—	—
	6 265.13	2.18	-2.55	96	33	50	70
	6 311.50	2.83	-3.23	32	—	—	—

Continued on next page

Table A1 – Continued

Element	Wavelength	χ (eV)	$\log gf$	Equivalent widths (mÅ)			
				HD 15096	HD 37792	HD 141804	HD 207585
	6 322.69	2.59	-2.43	78	23	35	—
	6 380.74	4.19	-1.32	53	15	25	33
	6 392.54	2.28	-4.03	21	—	—	—
	6 393.60	2.43	-1.43	—	71	88	102
	6 411.65	3.65	-0.66	—	61	77	93
	6 419.95	4.73	-0.09	89	36	49	59
	6 421.35	2.28	-2.01	122	61	77	94
	6 430.85	2.18	-2.01	124	61	74	93
	6 436.41	4.19	-2.46	12	—	—	—
	6 469.19	4.83	-0.62	56	16	29	40
	6 518.37	2.83	-2.30	71	14	—	—
	6 551.68	0.99	-5.79	11	—	—	—
	6 574.23	0.99	-5.02	39	—	—	17
	6 592.91	2.72	-1.47	126	54	—	94
	6 593.87	2.44	-2.42	89	33	46	67
	6 597.56	4.79	-0.92	45	—	17	29
	6 608.03	2.28	-4.03	23	—	—	—
	6 609.11	2.56	-2.69	69	15	29	46
	6 646.93	2.61	-3.99	14	—	—	—
	6 699.14	4.59	-2.19	10	—	—	—
	6 703.57	2.76	-3.16	38	—	—	22
	6 710.32	1.80	-4.88	14	—	—	—
	6 713.74	4.79	-1.60	19	—	—	11
	6 739.52	1.56	-4.95	58	—	—	30
	6 750.15	2.42	-2.62	82	27	38	56
	6 752.71	4.64	-1.20	39	—	18	26
	6 783.70	2.59	-3.98	15	—	—	—
	6 793.26	4.07	-2.47	14	—	—	—
	6 806.85	2.73	-3.21	40	—	—	17
	6 810.26	4.61	-0.99	49	14	—	26
	6 820.37	4.64	-1.17	41	—	17	25
	6 841.34	4.61	-0.60	70	22	32	—
	6 858.15	4.61	-0.93	51	—	28	—
Fe II	4 993.35	2.81	-3.67	31	25	28	41
	5 132.66	2.81	-4.00	17	—	—	—
	5 197.56	3.23	-2.25	64	—	—	—
	5 234.62	3.22	-2.24	66	84	74	83
	5 284.10	2.89	-3.01	51	—	49	63
	5 325.56	3.22	-3.17	29	34	32	38
	5 414.05	3.22	-3.62	16	19	20	—
	5 425.25	3.20	-3.21	31	33	34	49
	5 534.83	3.25	-2.77	43	55	45	—
	5 991.37	3.15	-3.56	21	21	22	30
	6 084.10	3.20	-3.80	12	15	14	21
	6 149.25	3.89	-2.72	22	29	26	35

Continued on next page

Table A1 – Continued

Element	Wavelength	χ (eV)	$\log gf$	Equivalent widths (mÅ)			
				HD 15096	HD 37792	HD 141804	HD 207585
	6 247.55	3.89	-2.34	34	52	47	53
	6 416.92	3.89	-2.68	27	27	32	33
	6 432.68	2.89	-3.58	—	32	—	38

Table A2. Atomic line lists for other chemical species.

Element	Wavelength	χ (eV)	$\log gf$	Ref	Equivalent widths (mÅ)			
					HD 15096	HD 37792	HD 141804	HD 207585
C I	4 770.03	7.48	-2.33	T02	—	17	22	21
	4 775.90	7.49	-2.19	T02	11	22	30	—
	4 932.05	7.69	-1.66	T02	—	33	53	—
	5 052.10	7.68	-1.30	T02	26	49	67	70
	5 380.34	7.68	-1.84	T02	—	33	43	45
	6 587.60	8.54	-1.22	L82	—	27	—	38
	7 111.48	8.64	-1.32	L82	—	17	—	24
	7 113.18	8.64	-0.95	L82	—	30	43	37
	7 115.19	8.64	-0.90	L82	—	30	40	47
	7 116.99	8.64	-1.08	L82	—	25	32	37
	9 061.48	7.48	-0.34	TS97	—	—	177	—
9 078.32	7.48	-0.58	TS97	—	160	—	156	
9 111.85	7.49	-0.29	TS97	105	—	—	—	
O I	7 771.94	9.15	+0.32	TH05	—	126	89	73
	7 774.16	9.15	+0.17	TH05	—	111	75	68
	7 775.35	9.15	-0.04	TH05	—	88	63	61
Na I	5 682.65	2.10	-0.70	PS	96	48	63	79
	5 688.22	2.10	-0.40	PS	125	68	86	104
	6 154.22	2.10	-1.57	R03	39	13	15	24
	6 160.75	2.10	-1.27	R03	65	19	25	39
Mg I	4 571.10	0.00	-5.57	N96	124	46	67	86
	4 702.99	4.35	-0.38	N96	—	144	—	—
	4 730.04	4.34	-2.39	R03	78	25	35	41
	5 528.42	4.34	-0.36	J2006	—	139	—	—
	5 711.10	4.34	-1.68	R99	118	54	66	81
	6 318.71	5.11	-1.94	Ca2007	—	10	—	—
	8 712.69	5.93	-1.26	Ca2007	65	—	—	—
	8 717.83	5.91	-0.97	WSM	84	—	—	—
	8 736.04	5.94	-0.34	WSM	—	78	91	—
Al I	6 696.03	3.14	-1.48	MR94	39	—	11	19
	6 698.67	3.14	-1.63	R03	29	—	—	11
	7 835.32	4.04	-0.580	R03	42	—	19	20
	7 836.13	4.02	-0.400	R03	57	—	21	25
	8 772.88	4.02	-0.250	R03	79	—	—	—
	8 773.91	4.02	-0.070	R03	93	—	—	—

Continued on next page

Table A2 – Continued

Element	Wavelength	χ (eV)	$\log gf$	Ref	Equivalent widths (mÅ)			
					HD 15096	HD 37792	HD 141804	HD 207585
Si I	5 793.08	4.93	-2.06	R03	37	—	—	32
	6 125.03	5.61	-1.54	E93	29	12	19	25
	6 131.58	5.62	-1.69	E93	21	—	13	—
	6 145.08	5.62	-1.43	E93	33	12	20	26
	6 155.14	5.62	-0.77	E93	—	40	—	—
	8 728.01	6.18	-0.36	E93	—	47	—	—
	8 742.45	5.87	-0.51	E93	89	60	—	—
Ca I	5 581.80	2.52	-0.67	C2003	104	47	63	77
	5 601.29	2.52	-0.52	C2003	125	—	70	88
	5 857.46	2.93	+0.11	C2003	145	79	87	100
	5 867.57	2.93	-1.61	C2003	—	—	—	12
	6 102.73	1.88	-0.79	D2002	—	—	86	99
	6 122.23	1.89	-0.32	D2002	—	101	121	132
	6 161.30	2.52	-1.27	E93	—	18	26	43
	6 162.18	1.90	-0.09	D2002	—	119	130	151
	6 166.44	2.52	-1.14	R03	77	29	34	46
	6 169.04	2.52	-0.80	R03	103	40	53	64
	6 169.56	2.53	-0.48	DS91	123	55	71	81
	6 439.08	2.52	+0.47	D2002	—	106	—	—
	6 449.82	2.52	-0.50	C2003	—	56	79	78
	6 455.60	2.51	-1.29	R03	63	17	23	37
	6 464.68	2.52	-2.42	C2003	15	—	—	—
	6 471.66	2.51	-0.69	S86	96	49	64	69
	6 493.79	2.52	-0.11	DS91	—	80	88	100
6 499.65	2.52	-0.81	C2003	92	39	52	65	
6 717.69	2.71	-0.52	C2003	—	52	66	82	
Ti I	4 512.740	0.840	-0.400	L13	80	—	33	52
	4 518.030	0.830	-0.250	L13	87	25	38	54
	4 533.249	0.850	+0.540	L13	—	61	72	85
	4 534.785	0.840	+0.350	L13	—	50	67	80
	4 548.770	0.830	-0.281	L13	80	22	37	54
	4 555.490	0.850	-0.400	L13	74	20	36	—
	4 617.280	1.750	+0.439	L13	—	18	32	46
	4 639.950	1.740	-0.190	L13	54	—	13	26
	4 758.120	2.250	+0.510	L13	54	14	16	28
	4 759.280	2.250	+0.590	L13	55	12	19	29
	4 778.260	2.240	-0.351	L13	21	—	—	—
	4 981.718	0.840	+0.570	L13	—	68	—	—
	4 981.740	0.850	+0.570	L13	—	—	80	98
	5 016.170	0.850	-0.480	L13	—	14	29	—
	5 022.870	0.830	-0.331	L13	—	25	—	56
	5 039.960	0.020	-1.080	L13	92	—	—	—
	5 043.590	0.840	-1.590	L13	33	—	—	—
5 145.470	1.460	-0.539	L13	56	—	—	24	

Continued on next page

Table A2 – Continued

Element	Wavelength	χ (eV)	$\log gf$	Ref	Equivalent widths (mÅ)			
					HD 15096	HD 37792	HD 141804	HD 207585
	5 152.190	0.020	-1.950	L13	—	—	—	17
	5 173.750	0.000	-1.060	L13	—	28	—	—
	5 210.390	0.050	-0.821	L13	—	32	53	74
	5 219.710	0.020	-2.220	L13	43	—	—	—
	5 295.780	1.050	-1.590	L13	23	—	—	—
	5 490.160	1.460	-0.840	L13	33	—	—	—
	5 866.460	1.070	-0.790	L13	65	10	17	26
	5 922.120	1.050	-1.380	L13	32	—	—	10
	6 091.180	2.270	-0.320	L13	20	—	—	—
	6 126.220	1.050	-1.370	R03	36	—	—	—
	6 258.110	1.440	-0.390	L13	61	—	17	31
	6 261.100	1.430	-0.530	L13	63	—	15	27
Cr I	4 254.346	0.000	-0.090	S07	—	127	—	—
	4 289.729	0.000	-0.370	S07	—	—	141	—
	4 789.340	2.540	-0.330	S07	—	—	38	—
	4 936.340	3.110	-0.250	S07	—	12	17	—
	5 206.044	0.940	+0.020	S07	—	—	123	—
	5 247.570	0.960	-1.590	S07	—	22	38	60
	5 296.690	0.982	-1.360	S07	104	34	—	75
	5 300.750	0.980	-2.000	S07	—	13	—	—
	5 345.800	1.003	-0.950	S07	127	56	77	—
	5 348.330	1.000	-1.210	S07	104	38	—	73
	5 409.800	1.030	-0.670	S07	—	67	84	106
	5 787.930	3.322	-0.080	R03	50	—	21	27
	6 330.097	0.940	-2.920	R03	39	—	—	—
Ni I	4 519.982	1.676	-3.080	W14	38	—	—	—
	4 604.988	3.479	-0.240	W14	84	—	—	—
	4 756.515	3.479	-0.270	W14	76	—	—	—
	4 866.271	3.538	-0.220	W14	75	—	—	—
	4 953.210	3.740	-0.580	W14	53	19	29	37
	4 976.326	1.676	-3.000	W14	43	—	—	—
	5 010.940	3.635	-0.979	W14	—	17	22	33
	5 084.110	3.680	-0.180	E93	88	47	—	70
	5 115.400	3.834	-0.280	R03	66	36	45	—
	5 578.730	1.677	-2.830	W14	—	13	22	—
	5 587.870	1.935	-2.390	W14	57	—	—	46
	5 748.360	1.677	-3.240	W14	31	—	—	—
	6 108.120	1.677	-2.600	W14	62	—	—	46
	6 128.980	1.677	-3.429	W14	25	—	—	—
	6 176.820	4.089	-0.264	R03	58	21	29	43
	6 177.250	1.826	-3.460	W14	15	—	—	—
	6 204.610	4.089	-1.080	W14	19	—	—	—
	6 223.990	4.106	-0.910	W14	22	—	10	—
	6 327.600	1.677	-3.170	W14	42	—	13	24

Continued on next page

Table A2 – Continued

Element	Wavelength	χ (eV)	$\log gf$	Ref	Equivalent widths (mÅ)			
					HD 15096	HD 37792	HD 141804	HD 207585
	6 532.873	1.935	-3.350	W14	22	—	—	—
	6 586.330	1.950	-2.780	W14	43	—	14	24
	6 643.640	1.676	-2.220	W14	—	—	46	—
	6 767.770	1.830	-2.140	W14	82	—	—	—
	6 772.320	3.658	-0.970	R03	47	14	21	32
Sr I	4 607.33	0.00	+0.28	SN96	106	36	73	85
Y II	4 883.68	1.08	+0.07	SN96	101	83	108	127
	5 087.43	1.08	-0.17	SN96	83	73	91	105
	5 200.41	0.99	-0.57	SN96	71	61	80	92
	5 205.72	1.03	-0.34	SN96	—	70	87	94
	5 289.81	1.03	-1.85	R04	22	13	24	38
	5 402.78	1.84	-0.44	R03	40	27	53	61
Zr II	4 050.32	0.71	-1.06	Lj06	50	39	59	69
	4 208.99	0.71	-0.51	Lj06	70	71	77	93
	4 210.61	1.66	-1.19	Lj06	—	—	23	37
	4 317.32	0.71	-1.46	Lj06	—	29	55	66
	4 613.95	0.97	-1.54	Lj06	—	—	42	—
	5 112.27	1.66	-0.85	Lj06	37	17	44	60
	5 350.35	1.77	-1.16	Lj06	23	—	30	45
La II	5 303.53	0.32	-1.35	L01a	20	6	26	42
	5 805.77	0.13	-1.56	L01a	24	8	29	42
	6 262.29	0.40	-1.22	L01a	31	13	42	76
	6 320.43	0.17	-1.52	SN96	19	—	29	44
	6 774.33	0.13	-1.71	VWR	14	—	26	41
Ce II	4 418.79	0.86	+0.27	L09	—	24	58	—
	4 483.90	0.86	+0.10	L09	—	—	50	—
	4 486.91	0.29	-0.18	L09	49	29	55	66
	4 539.74	0.33	-0.08	L09	—	—	64	—
	4 560.96	0.48	-0.26	L09	—	—	44	—
	4 562.37	0.48	+0.21	L09	52	44	69	77
	5 187.45	1.21	+0.17	L09	27	13	39	—
	5 274.24	1.04	+0.13	L09	30	19	43	53
	5 330.58	0.87	-0.40	L09	16	12	30	40
	5 393.39	1.10	-0.06	L09	26	—	36	—
	5 975.82	1.33	-0.45	L09	—	—	19	25
	6 043.37	1.21	-0.48	L09	10	—	19	27
Nd II	4 706.54	0.00	-0.71	DH	—	27	50	—
	4 763.62	0.38	-1.27	DH	10	—	—	—
	4 777.72	0.38	-1.22	DH	—	—	23	—
	4 797.15	0.56	-0.69	DH	—	10	—	—
	4 825.48	0.18	-0.42	DH	—	28	—	—
	4 902.04	0.06	-1.34	DH	—	—	25	—
	4 914.38	0.38	-0.70	DH	26	—	39	46

Continued on next page

Table A2 – Continued

Element	Wavelength	χ (eV)	$\log gf$	Ref	Equivalent widths (mÅ)			
					HD 15096	HD 37792	HD 141804	HD 207585
	5 063.72	0.98	-0.62	DH	—	—	19	32
	5 092.80	0.38	-0.61	DH	28	12	36	50
	5 212.36	0.20	-0.96	DH	—	11	33	47
	5 249.58	0.98	+0.20	DH	34	31	—	—
	5 255.51	0.20	-0.67	DH	—	—	—	55
	5 293.16	0.82	+0.10	DH	—	22	51	63
	5 306.46	0.86	-0.97	DH	—	—	—	20
	5 311.46	0.98	-0.42	DH	19	—	—	38
	5 319.81	0.55	-0.14	DH	39	—	55	65
	5 356.97	1.26	-0.28	DH	—	—	21	—
	5 371.93	1.41	-0.00	DH	—	—	32	—
	5 485.70	1.26	-0.12	DH	—	—	28	—
	5 740.88	1.16	-0.53	DH	10	—	15	23
	5 811.57	0.86	-0.86	DH	—	—	14	—
Sm II	4 318.94	0.28	-0.25	L06	—	—	—	47
	4 360.71	0.25	-0.87	L06	—	16	—	—
	4 362.02	0.48	-0.47	L06	—	19	—	—
	4 467.34	0.66	+0.15	L06	34	—	42	50
	4 499.48	0.25	-0.87	L06	15	—	19	32
	4 523.91	0.43	-0.39	L06	—	—	—	36
	4 566.20	0.33	-0.59	L06	22	—	22	39
	4 676.90	0.04	-0.87	L06	—	—	23	—
	4 704.40	0.00	-0.86	L06	24	—	29	39
	4 791.60	0.10	-1.44	L06	—	—	10	14

NOTES—References: (C2003) Chen et al. (2003); (Ca2007) Carretta et al. (2007); (D2002) Depagne et al. (2002); (DH) Den Hartog et al. (2003); (DS91) Drake & Smith (1991); (E93) Edvardsson et al. (1993); (J2006) Johnson et al. (2006); (L01) Lawler et al. (2001a); (L06) Lawler et al. (2006); (L09) Lawler et al. (2009); (L13) Lawler et al. (2013); (L82) Lambert et al. (1982); (Lj06) Ljung et al. (2006); (MR94) McWilliam & Rich (1994); (N96) Norris et al. (1996); (PS) Preston & Sneden (2001); (R03) Reddy et al. (2003); (R04) Reyniers et al. (2004); (R99) Reddy et al. (1999); (S07) Sobeck et al. (2007); (S86) Smith et al. (1986); (SN96) Sneden et al. (1996); (T02) Takeda et al. (2002); (TH05) Takeda & Honda (2005); (TS97) Takeda & Sadakane (1997); (VWR) Van Winckel & Reyniers (2000); (W14) Wood et al. (2014); (WSM) Wiese et al. (1969).